Version of Record: https://www.sciencedirect.com/science/article/pii/S0926337319311324
Manuscript_7a2f4d7e622d6e2ee1160de67ebf535c

Photo-generated Reactive Oxygen Species Assisted Tandem Amine Homocoupling and Amine-alcohol Cross-coupling Reaction on Mesoporous Spinel Cobalt Oxide

Tharindu Kankanam Kapuge[†], Wimalika R. K. Thalgaspitiya[†], Dinithi Rathnayake[†], Junkai He[‡], Peter Kerns[†], Steven L. Suib*[†‡]
[†]Department of Chemistry, University of Connecticut, Storrs, CT 06269, USA
[‡]Institute of Material Science, University of Connecticut, Storrs, CT 06269, USA

*steven.suib@uconn.edu

Keywords - Mesoporous, cobalt oxide, surfactant, singlet oxygen, hydroxyl radical, benzylamine, alcohol, photocatalyst

Abstract

Mesoporous spinel cobalt oxide (Co_3O_4) with fine-tuned pore size distributions (9.6-17.6 nm) and different surface areas (33-85 m^2/g) were synthesized using a series of nonionic surfactants. A direct influence of the chemical composition of the surfactants and calcination temperature on crystallite size, morphology, pore size/ volume, surface area, valance band edge, and Co^{2+}/ Co^{3+} ratio was recognized. Correlation between the aforementioned factors, transition metal ion incorporation and benzylamine homocoupling reaction was discussed. Shape-specific binding of amine on the cobalt oxide active sites was proposed based on substrate scope study. Tandem synthesis strategy to selectively synthesize amine (aliphatic/aromatic) homo-coupled imines and amine-alcohol cross-coupled imines was introduced. Low-intensity light-induced singlet oxygen and hydroxyl radical-mediated reaction mechanism was proposed based on the EPR, XPS, photoreactor, and reactive oxygen species scavenger tests. Selective and switchable synthesis of homo-coupled (yield 85%) and cross-coupled (yield 87%) products was achieved with sodium azide and mannitol additives.

© 2019 published by Elsevier. This manuscript is made available under the Elsevier user license
https://www.elsevier.com/open-access/userlicense/1.0/

Introduction

Carbon-heteroatom (N, O, S) bond formation is considered as the backbone of synthetic organic chemistry. Amine homocoupling[1], amine-alcohol cross-coupling[2], and amine-carbonyl condensation[3] reactions have been utilized in C-N bond (Schiff base) formation strategies. The traditional amine-carbonyl condensation reactions have been recently replaced with much greener amine-amine homocoupling and amine-alcohol cross coupling reactions.[4,5] Metal oxides, complexes (Cu, Fe, Al, V, Ce, Mn, Pd, Au, Ag, Ir, Ru, Pt), and metal free (bases, graphite, TEMPO) catalytic systems have been used in the oxidation of amines-alcohols to imines.[6] These synthesized secondary imines can be further transformed into various pharmaceutically important compounds such as aziridines, β-lactams, benzimidazole, and benzoxazole.[7,8] According to one of the widely accepted reaction mechanisms of secondary imine formation, during both alcohol-amine and amine-amine coupling reactions, alcohols or amines are first oxidized to their respective aldehydes (amine can also converted to primary imine which then react directly with excess amine to form secondary imine) which are then reacted with unreacted amine to form the secondary imine.[9] If both alcohols and amines are in the same reaction mixture, a catalyst which can selectively dehydrogenate the alcohol or the amine can be used to modulate the homo- and hetero-coupled product yields.

The above mentioned alcohol and amine dehydrogenation reactions have been separately studied in the literature. A Mars-van Krevelen type reaction mechanism was proposed for alcohol oxidation (oxidative dehydrogenation, ODH) on manganese dioxide by Suib et al. in 2002.[10] Lattice oxygens of manganese dioxide abstract protons from the organic substrate (alcohol) to form intermediate reactive oxygen species (H_2O_2) and oxygen vacancies in the lattice. However, manganese dioxides cannot be used in the presence of complex organic substrates with oxidation susceptible substituent groups due to strong oxidizing ability of the catalyst[11,12] Mild ODH catalysts and reaction conditions (low temperature, photocatalyst) are required to mitigate the unnecessary side reactions. The most challenging task in the primary amine dehydrogenation is the prevention of the primary imine/aldehyde and excess amine coupling reaction.[13] It is essential to halt the reaction at the primary imine in order to facilitate the alcohol-amine cross coupling reaction. Design of a mild catalyst which can switch between alcohol ODH and amine ODH (lead to amine-alcohol and amine homocoupling respectively) is required for tandem one pot organic syntheses of imines.

Cobalt oxide has been extensively used in CO oxidation[14], Fisher-Tropsch[15], and oxygen and hydrogen evolution[16] reactions as an efficient catalyst. Applications of cobalt oxide in heterogenous organic catalysis have been limited to few fundamentally similar reactions such as alcohol oxidation[17] and nitrogen heterocycle dehydrogenation[18]. The alcohol oxidation ability of cobalt complexes had been previously utilized in alcohol-amine cross coupling in homogenous reaction conditions.[19] Similar reactions have been carried out in the presence of heterogenous precious metal (Pt, Au, Pd) catalysts.[20,21] However, one-pot, tandem imine formation from switchable pathways (amine homocoupling and amine-alcohol cross-coupling) have not been reported in the literature.

Effects of physiochemical properties such as particle size[22], lattice strain[23], oxygen vacancies[23], surface area[24], pore diameter[25], and electronic environment of cobalt-based catalysts on CO oxidation, Fisher-Tropsch, and OER/HER reactions have been investigated in separate studies. Catalyst structure-activity relationship studies on imine formation reactions are uncommon or limited to few physical properties. Understanding the relationship between the structural features of a catalyst and its chemical reactivity is vital in new catalyst design. Photo-mediated carbon-heteroatom coupling which is important from a sustainable standpoint have been extended to imine formation reactions over the last decade. Various visible and ultraviolet photocatalytic systems including but not limited to functionalized TiO_2, Zn_6Ti,CdS, C_3N_4 and corresponding mechanisms of amine homocoupling reactions have been investigated.[6] Photo-mediated control of amine homocoupling and amine-alcohol cross coupling reactions has not gained great attention to date.

A thorough characterization of spinel cobalt oxide (Co_3O_4) synthesized under different nonionic surfactants was carried out in order to understand the effects of surfactants on physiochemical properties of the catalysts in the first section of this report. The above catalysts were used to drive the photo-mediated benzylamine homocoupling reaction in the absence of the alcohol and the catalyst structure-activity relationship is discussed in the next section. In the third part, the above reaction was carried out in the presence of alcohols and one-pot benzylamine homo-coupling and benzylamine-alcohol cross-coupling reactions were optimized. This one-pot strategy would be useful in controlling reactions involving reactants with amine and alcohol groups in the same molecule. In the last section, the reaction mechanisms were investigated in order to further identify the involvement of cobalt oxide lattice and molecular oxygen in the reaction.

Methodology

1. Catalyst synthesis

Synthesis of spinel cobalt oxide was done by modifying the general mesoporous metal oxide synthesis approach reported by Suib et. al.[26] All chemicals were purchased from Sigma Aldrich and used without any pretreatment. In general synthesis, 5.0 g of $Co(NO_3)_2.6H_2O$ was dissolved in 17.0 g of anhydrous butanol followed by addition of 2.4 g of 70% nitric acid and 2.5 g surfactant. Synperonic F108, Span 80, Tween 80, Birj 58, PEG-400, and P123 which were labeled as A thru E and P123 were used as surfactants. Solutions were kept in a convection oven at 120°C until foam appears in beakers. Samples were cooled down and dispersed in 120 mL of ethanol. Solutions were centrifuged at 7000 rpm for 5 minutes followed by overnight vacuum drying. The pink-colored powder was calcined at the desired temperatures (250°C, 350°C) in a box furnace for 2 hours. Transition metal ion incorporation was done by adding (5% wt. based on cobalt precursor) transition metal ion precursors to the butanol solution along with cobalt nitrate. Similarly, 5% wt. graphene oxide slurry (prepared in section 3) was added during the graphene-CO_3O_4 synthesis. Copper(II) nitrate hexahydrate, manganese(II) nitrate tetrahydrate, zinc(II) nitrate hexahydrate, nickel(II) nitrate hexahydrate, palladium(II) nitrate dihydrate, molybdenum(V) chloride were used as transition metal precursors in the incorporation. Materials have been labeled using the following notation. Surfactant-Co_3O_4-calcination temperature (eg: A- Co_3O_4-350).

2. Synthesis of graphene oxide (GO)

A modified Hummer's method was used to synthesize graphene oxide from graphite. In a typical synthesis, 1 g of graphite and 1 g of $NaNO_3$ were added to 50 mL of concentrated H_2SO_4 in an ice bath followed by stirring for 30 minutes. Then, 8 g of $KMnO_4$ was added to the mixture. The resultant green solution was further stirred for 30 minutes in the ice bath and was transferred into a 40°C water bath. To ensure the complete oxidation of graphite layers, the solution mixture was stirred for another 90 minutes. Then, 100 mL of distilled water was added slowly to the solution followed by stirring for 30 minutes. After that, 12 mL of 30% hydrogen peroxide was added to the solution mixture to quench the reaction. Finally, 100 mL of distilled water was added to the golden-brown sol which resulted in a brown gel-like precipitate. The precipitate, graphene oxide, was washed with distilled water until the pH was neutral.

3. Cyclic voltammetry

Active materials containing working electrodes were prepared as follows. About 16 mg of cobalt oxide was ground with 4 mg of graphite until the mixture became a homogenous fine powder. Eight mg of powder was sonicated with 50 μL Nafion solution, 250 μL water, and 250 μL ethanol for 1 hour. The ink mixture was stirred for additional 1 hour before the loading step. Fifty μL of the ink was homogenously drop casted on 1 cm× 1 cm area of a 1 cm×2 cm carbon paper. The paper was dried under slow flow of house nitrogen for 2 hours. A three-electrode cell with Pt counter electrode, CHI 152 (Hg/HgO) reference electrode, and working electrode was used to perform cyclic voltammetry experiments on a CHI electrochemical workstation.

Results

1. Material Characterization

X-ray diffraction (XRD) patterns corresponding to spinel cobalt oxide (Co_3O_4) were observed in all samples prepared with different surfactants as shown in **Figure 1** (left). The crystal structure was determined as cubic Co_3O_4 with Fd-3m (227) space group symmetry (PDF 01-080-1532, CSD 69365). The cubic unit cell dimension of a=8.0821Å was noticed after the refinement. Discrepancy in the full width at half maximum (FWHM) and peak position values were noticed in the samples prepared with different surfactants.

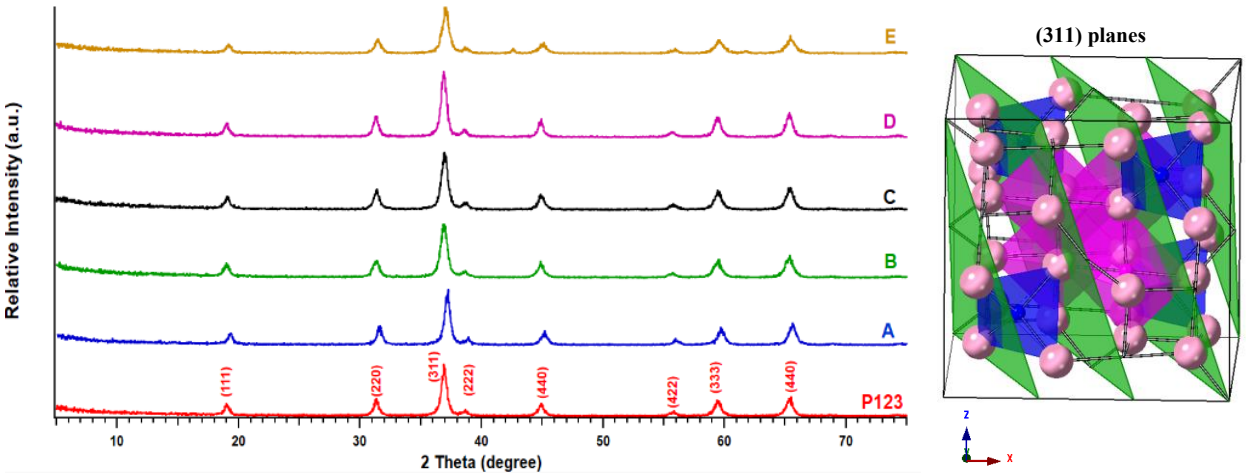

Figure 1. X-ray diffraction patterns of Co_3O_4 prepared with different surfactants (A-Synperonic F108, B-Span 80, C-Tween 80, D-Birj 58, E-PEG-400, and P123; for structural information see **Figure S1**) and calcined at 350°C (left). The cubic Co_3O_4 unit cell showing octahedral Co(III) sites (purple), tetrahedral Co(II) sites (blue), and planes parallel to (311) crystal planes (right)

Halder-Wagner (HW) and Williamson-Hall (WH) (without internal correction) calculations were performed to determine the crystallite sizes and micro-strains of each sample. The data were best described by the HW model **(Figure S2-S7)**. Highest peak intensity was observed in the peak corresponding to the (311) diffraction planes as shown in **Figure 1 (right).** A decrease in the HW crystallite sizes was noticed in the order of (17 nm) P123> A> D> E> C> B (13 nm) while the micro-strain decreased in the order of (0.4%) E> P123> B> A> D> C (0.1%) in 350°C calcined samples **(Figure S8 and S9)**. A spherical crystallite shape (shape factor ~1) was assumed when calculating the crystallite size using the HW model. Increase in the crystallite sizes (maximum 86%) were noticed as the calcination temperature was increased from 250°C to 350°C **(Table S1)**.

The smallest crystallite size deviation was seen in sample prepared with surfactant C while the highest deviation was observed in the sample B when the calcination temperature was increased from 250°C to 350°C.

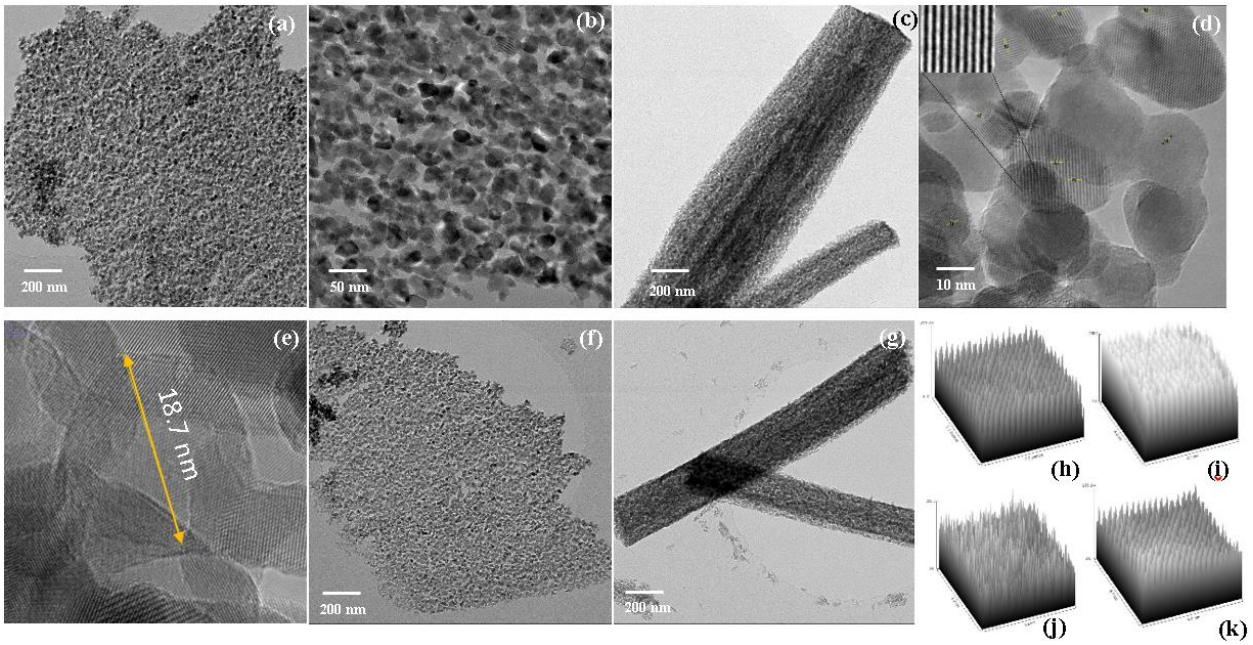

Figure 2. TEM images of (a) Co_3O_4-A-350 nano-sheet (b) Co_3O_4-A-350 nano-sheets composed of nano-crystallites (c) Co_3O_4-B-350 nanorods (d) Co_3O_4-B-350 crystallites (inset showing lattice fringes) (e) Co_3O_4 -B-350 spherical crystallite with ~19 nm diameter (f) Co_3O_4 -C-350 nanosheet (g) Co_3O_4 -D-350 nanorods (h, i, j, k) surface profiles showing surface irregularities of Co_3O_4 -A, B, C, D-350 respectively. (A-Synperonic, F108, B-Span 80, C-Tween 80, D-Birj 58, E-PEG-400, and P123)

Transmission electron microscopic (TEM) images were obtained using FEI Talos F200X TEM **(Figure 2).** Lattice fringes of Co_3O_4 can be observed in the high-resolution TEM image (inset **Figure 2d)**. The d spacings of crystallites were measured and compared with the XRD data. Lattice fringes corresponding to (111), (220), and (311) were observed in high-resolution TEM. At least eight diffraction rings were observed in the selective area diffraction (SEAD) pattern (**Figure S10**). Surface irregularities on the crystallite surfaces were examined as shown in **Figure 2(h-k)**. Most regular crystallite surfaces were noticed on the particles of sample B while the least regular surfaces were identified in samples C and E. Nano-crystallites were assembled to form sheets in samples A and C as shown in **Figure 2a and 2f** whereas nano-crystallites were assembled to form nanorods in samples B and D (**Fig. 2c, 2g**).

Scanning electron microscope (SEM) images were obtained with a Nova NanoSEM 450 to check the intact structures of particles (**Figure 3**). Similar morphology, aggregation of flakes, was observed in the particles of sample A-350 and P123-350. Particles with smooth surfaces compared to other samples can be seen in samples B-350 and D-350. Deviation of the morphology (wool ball) was observed in sample C-350. Highest average particle sizes (~5 μm) can be seen in samples C-350 and D-350 whereas smaller average particle sizes (< 2.8 μm) were noticed in other samples.

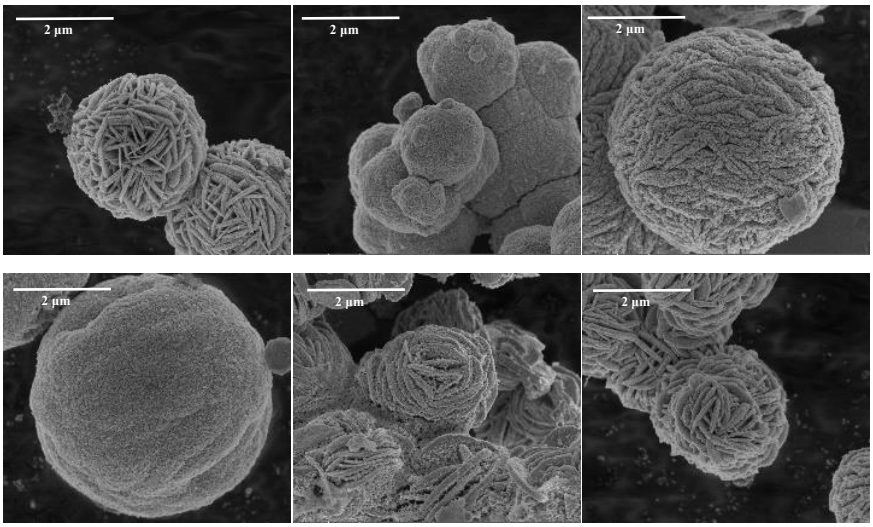

Figure 3. SEM images of Co_3O_4 samples prepared with different surfactants calcined at 350°C; top left to right (A-C), bottom left to right (D, E, and P123 (magnification 25000, scale 2 μm). (A-Synperonic F108, B-Span 80, C-Tween 80, D-Birj 58, E-PEG-400, and P123)

Nitrogen adsorption-desorption isotherms (**Figure 4**) of all six samples were obtained using a Quantachrome IQ automated gas sorption analyzer at 77K (liquid nitrogen) and the BJH pore volumes, pore diameters, and BET surface areas were calculated from isotherms (**Table 1**). Lowest pore diameter (7.8 nm) and volume (0.14 cc/g) were observed in sample E while the highest surface area (85 m^2/g) was depicted by sample B. Different BJH pore sizes were noticed in the range of 7.8 - 17.6 nm when different surfactants were used during the synthesis. Type IV isotherm with monomodal pore size distributions and H2b type hysteresis (**Figure 4 inset**) were observed in all samples except sample E in which the hysteresis was type H3

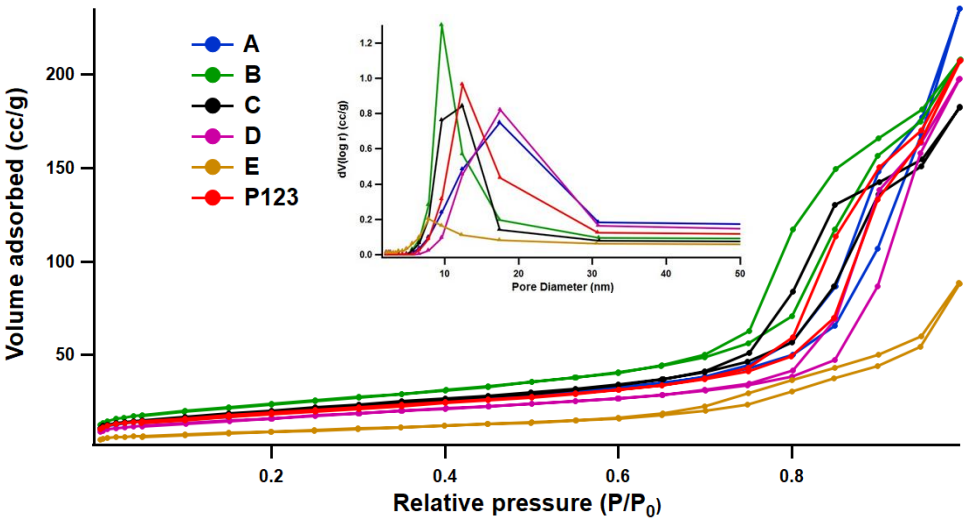

Figure 4. Nitrogen adsorption-desorption isotherms of Co_3O_4 samples prepared with different surfactants (A-E and P123) calcined at 350°C. (A-Synperonic F108, B-Span 80, C-Tween 80, D-Birj 58, E-PEG-400, and P123). Inset showing BJH pore size distribution.

Table 1. BJH pore volume, BJH pore diameter, and BET surface area of Co_3O_4-350 samples prepared with different surfactants (A-E and P123). (A-Synperonic F108, B-Span 80, C-Tween 80, D-Birj 58, E-PEG-400, and P123)

Sample	BJH pore volume (cc/g)	BJH pore diameter (nm)	BET surface area (m^2/g)
Co_3O_4-350-A	0.37	17.4	70
Co_3O_4-350-B	0.33	9.6	85
Co_3O_4-350-C	0.29	9.6	74
Co_3O_4-350-D	0.31	17.6	59
Co_3O_4-350-E	0.14	7.8	33
Co_3O_4-350-P123	0.33	12.4	68

The optical band gaps were calculated using diffuse reflectance solid UV visible spectroscopy (Shimadzu 2450). Diffuse reflectance data were converted to absorption data using the Kubelka-Munk transformation function ($F(R) = (1-R)^2/2R$ where R is the reflectance) and plotted against the wavelengths as shown in **Figure 5a**. Three distinct absorbance peaks were noticed in the UV (239 nm), visible (425 nm) and near IR (723 nm) regions. A modified function, $[(k/s)\ hv]^2$, was

constructed using $k/s=(1-R)^2/2R$ relationship where k-absorption coefficient, s-scattering coefficient and the function was plotted against the energy (eV) of photons. Four linear regions in the plots were extrapolated and the places where the lines intercept the x axis were considered as electronic transition edges. Four electronic transitions (3.8, 2.2, 2.0, and 1.5 eV) were observed in B-350°C sample as shown in **Figure 5b**. Electronic transition energies of all samples can be found in **Table S2.**

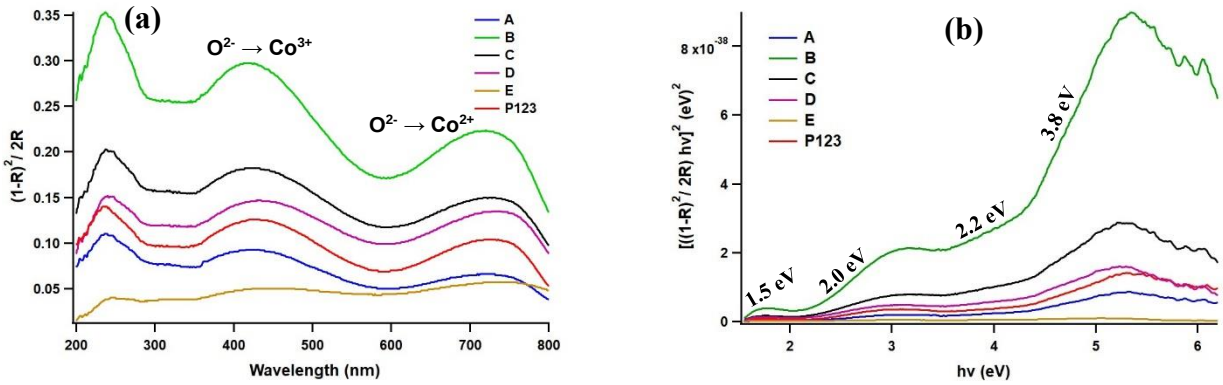

Figure 5. (a) Kubelka-Munk (b**)** modified Kubelka-Munk, transformed diffuse reflectance spectra of Co_3O_4 samples prepared with different surfactants (A-E and P123) calcined at 350°C. (A-Synperonic F108, B-Span 80, C-Tween 80, D-Birj 58, E-PEG-400, and P123)

Raman scattering spectra were obtained for six samples with a Renishaw system 2000 Raman spectrophotometer equipped with 514 nm laser. Four prominent peaks in the range of 185-189 cm^{-1}, 466-473 cm^{-1}, 507-517 cm^{-1}, 669-679 cm^{-1} and a weak peak near 615 cm^{-1} were observed as shown in **Figure 6**. Detailed Raman peak shifts were recorded in **Table S3**.

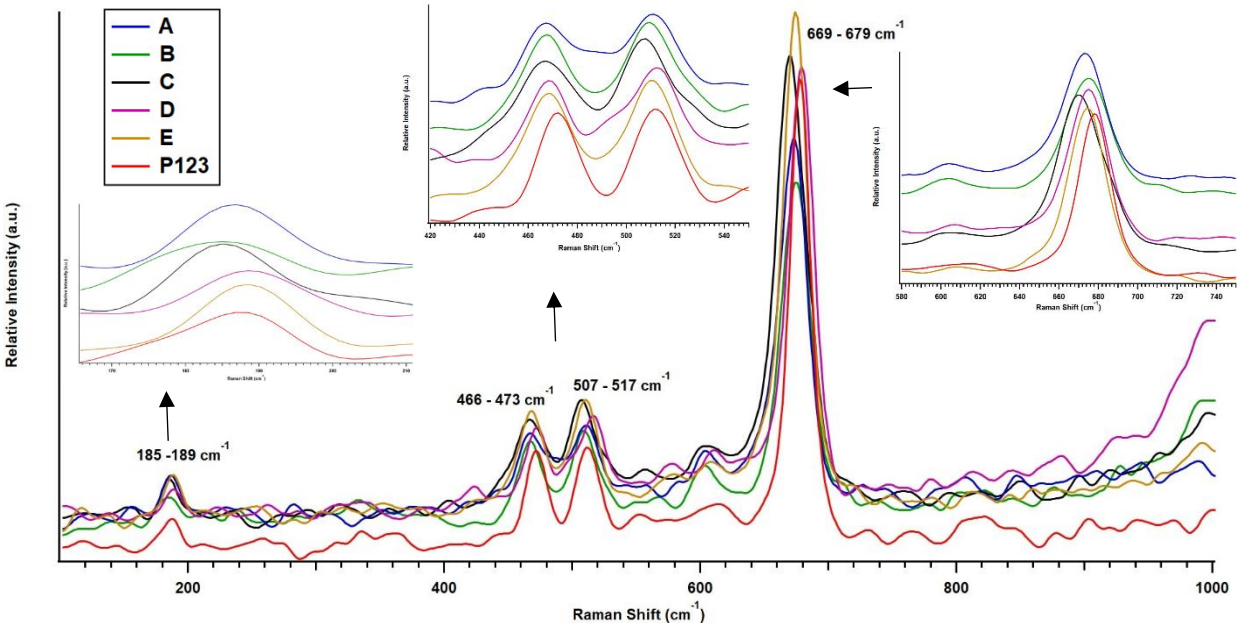

Figure 6. Raman scattering spectra of Co_3O_4 samples prepared with different surfactants (A-E and P123) inset showing zoomed in regions of spectra. (A-Synperonic F108, B-Span 80, C-Tween 80, D-Birj 58, E-PEG-400, and P123)

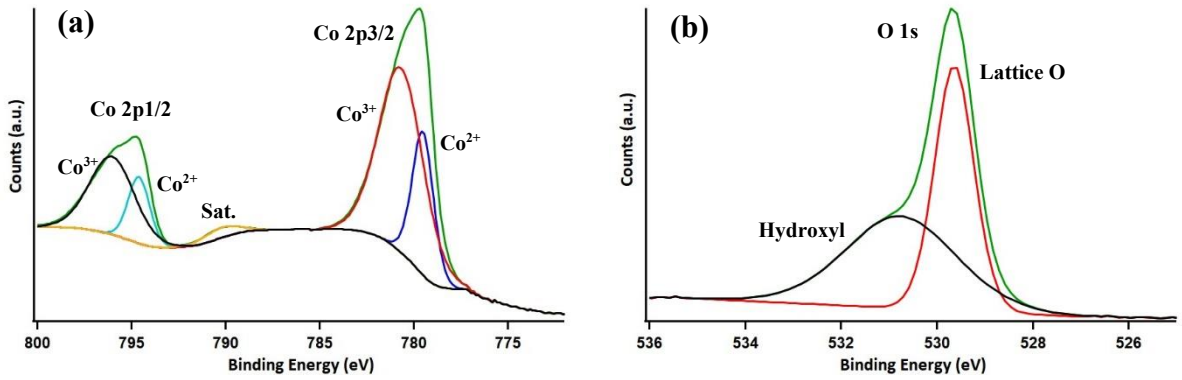

Figure 7. (a) Co 2p (b) O 1s high-resolution XPS spectra of Co_3O_4 prepared with surfactant B and calcined at 350°C (B-Span 80)

X-ray photoelectron spectroscopic (XPS) analysis was performed with a Physical Electronic Quantum 200 scanning ESCA microprobe with Al Kα radiation to determine chemical states of Co_3O_4 samples. Charge compensation was performed with adventitious carbon C1s peak at 284.8 eV. Two spin-orbit lines, Co $2p_{1/2}$ and $2p_{3/2}$, with 15.1 eV separation was recognized as shown in **Figure 7a**. Each spin-orbit line in Co 2p and O 1s spectra was best fit with two deconvolution peaks **(Figure 7b and 7b)**. Variations in peak shapes, positions, and areas of Co 2p and O 1s were

observed as tabulated in **Figure S13, Table S4-S6**. The peak to peak distances between Co^{2+} $2p_{1/2}$ and Co^{2+} $2p_{3/2}$ were in the range of 16.9 -15.6 eV whereas the Co^{3+} $2p_{1/2}$ to Co^{3+} $2p_{3/2}$ distances were in between 15.1 and 15.2 eV. Higher binding energy peak shifts were observed in O 1s spectra of A-350 and P123-350 samples. The Co^{2+} component was prominent compared to Co^{3+} in six samples. The ratios between the integrated peak areas of Co^{2+} and Co^{3+} were recorded in **Table S5**.

Cyclic voltammetry analyses of Co_3O_4 samples calcined at 350°C were performed with CHI electrochemical analyzer to determine the redox capability of samples. Details of electrode preparation procedure and three electrode system can be found in the methodology section. Two redox peaks with different potentials were observed in six catalysts at a scan rate of 20 mV/s as shown in **Figure 8.** Higher current density (capacitance) was observed in Sample E-350 and C-350 compared to other samples. Only one pair of redox peaks was observed in the CV and peaks separation corresponding to Co^{2+}/ Co^{3+} and Co^{3+}/Co^{4+} redox process was not observed.

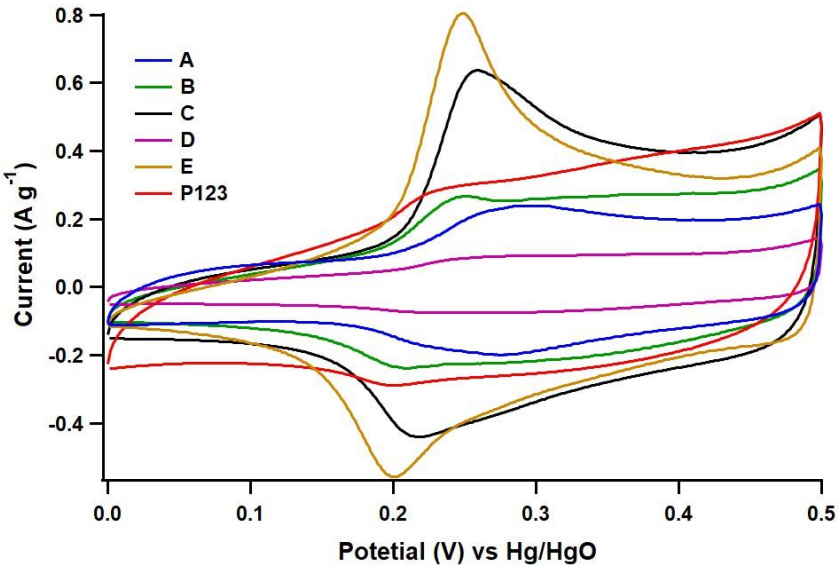

Figure 8. Cyclic voltammograms of Co_3O_4 prepared with different surfactants and calcined at 350°C. (A-Synperonic F108, B-Span 80, C-Tween 80, D-Birj 58, E-PEG-400, and P123). (three electrode system; platinum counter electrode, Hg/HgO reference electrode (CHI 152), active material deposited on carbon paper, 0.1 M KOH electrolyte, 20 mV/s).

2. Benzylamine homocoupling reaction

Cobalt oxide catalysts synthesized with different surfactants were used in the benzylamine homo-coupling reaction (**Figure 9**). The reaction conditions and analysis procedure can be found in the note sections of **Tables 2 and 3**. Reaction conversions were calculated using the GCMS peak areas of benzylamine, homo-coupled products, and calibration curve established using internal standard diphenylmethane. Blank reactions required to prove the true catalytic nature of Co_3O_4 were reported in **Table S7**. Highest homo-coupled product yield (among 350°C calcined catalysts) of 91% was observed when Co_3O_4-B-350 was used in the reaction as shown in **Table 2**. Overall higher product yields (>80%) were observed when 250°C calcined samples were used (except Co_3O_4-B (44%) and E (21%)) as depicted in **Table S8**.

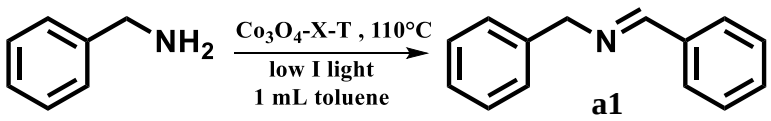

Figure 9. Benzylamine homo-coupling reaction catalyzed by cobalt oxide. Catalyst notation showing X-surfactant, T-calcination temperature, I -intensity

Highest homo-coupled product yields (among 250°C) were observed in both Co_3O_4-A-250 and Co_3O_4-D-250. Lowest catalytic activities were exhibited by catalyst E regardless of the calcination temperature.

Table 2. Benzylamine homocoupling to N-benzylbenzylimine with Co_3O_4-350 catalyst prepared with different surfactants. (A-Synperonic F108, B-Span 80, C-Tween 80, D-Birj 58, E-PEG-400, and P123)

Catalyst	**Conv. (%)**	**Sel. (%) (a1)**	**Yield (%) (a1)**	**TON**	**TOF**$\times 10^{-2}$ (h^{-1})
Co_3O_4-350-A	66	65	43	1.59	6.6
Co_3O_4-350-B	>99	92	91	2.38	9.9
Co_3O_4-350-C	67	66	44	1.61	6.7
Co_3O_4-350-D	71	70	50	1.70	7.1
Co_3O_4-350-E	27	26	7	0.65	2.7
Co_3O_4-350-P123	60	59	35	1.44	6.0

Reaction conditions - 10 mg catalyst, 1 mL toluene, 110°C, 24 hours, 0.1 mmol benzylamine, 4 mL PTFE capped sealed glass vessels, under normal room light, TON - moles of benzylamine converted per mole of catalyst, TOF - moles of benzylamine converted per mole of catalyst per hour. Diphenylmethane was used as an internal standard to determine the GCMS standard error. Sel. -selectivity, con. -conversion

Reactions were carried out in different solvents for 18 h while maintaining other reaction conditions similar to the conditions given in **Table 3**. Non-polar (toluene), polar protic (1-butanol), polar aprotic (dimethylacetamide [DMAc]), competitive substrate/solvent (cyclohexanone), and solvent-free conditions were investigated with Co_3O_4-X-350 catalysts (**Figure S14**). Highest product yields were observed when dimethylacetamide was used as the solvent. A completely different catalytic activity trend was observed under Co_3O_4-B-350. Low homocoupling product yields (<25%) were observed in butanol with all catalysts except Co_3O_4-B-350 (>70%). Butanol-benzylamine cross-coupled product was observed when butanol was used as the solvent. Even though intrinsically poor product yields were observed in solvent-free condition (500 μL benzylamine), the highest product yield was recorded for catalyst B-350. Significant homocoupling product yields (20-40%) were noticed with A-350 and B-350 even in the presence of competitive reactant, cyclohexanone. Catalyst Co_3O_4-A-350 was selected for the rest of the study.

Table 3. The substrate scope of homocoupling of benzylamine to N-benzylbenzylimine with Co_3O_4-350-B; (B-Span 80)

Substrate	Products		Con. %	Sel. a1 (%)	Sel. b (%)	Yield a1 (%)	TOF×10^{-2} (h^{-1})
	a	b					
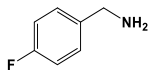	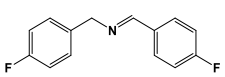	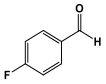	96	93	1	89	9.6
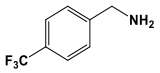	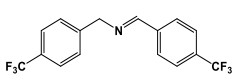	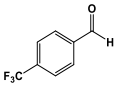	99	84	16	83	9.9
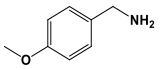	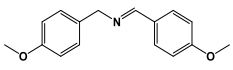	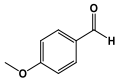	99	97	3	96	9.9
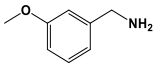	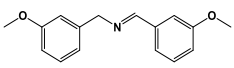	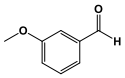	76	75	n/a	57	7.6
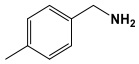	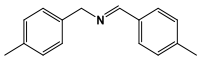	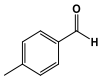	99	93	6	92	9.9
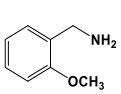	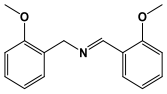		86	86	n/a	74	8.6

Reaction conditions - 10 mg Co_3O_4-350-B, 1 mL toluene, 110°C, 24 hours, 0.1 mmol substituted benzylamine, 4 mL PTFE capped sealed glass vessels, under normal room light, TON - moles of benzylamine converted per mole of catalyst, TOF - moles of benzylamine converted per mole of catalyst per hour. Diphenylmethane was used as an internal standard to determine the GCMS standard error. Sel. -selectivity, con. -conversion, n/a - not applicable

Effect of electron donating-withdrawing substitute groups and steric hindrance on the reaction performance was studied using different substituent groups attached to the benzylamine aromatic ring as shown in **Table 3**. Higher product yields were observed with moderate activator o, p-methoxy substituted benzylamine (74% and 96% respectively) compared to m-methoxy substituted reactant (57%). Similar high yields were noticed with both weak activator methyl group (92%) and strong deactivator trifluoromethyl group (83%). The selectivity towards intermediate benzaldehyde was increased in the case of the strong electron withdrawing trifluoromethyl group (16%) compared to the methyl group (6%). Following yield trend can be summarized based on the data in **Table 3**, m-OCH_3 < o-OCH_3 < CF_3 < F < CH_3 < p-OCH_3.

Table 4. Effect of cobalt oxide photoexcitation on homo-coupling of benzylamine reaction

Catalyst / Condition	Temperature (°C)	Reaction time (hours)	Conversion (%)	Selectivity (%) (a1)	Yield (%) (a1)	TON	TOF $\times 10^{-2}$ (h^{-1})
no cat. /dark	25	24	4	4	0.2	0.1	0.4
Co_3O_4-350 B/dark	25	24	6	6	0.3	0.1	0.6
Co_3O_4-350-B/dark	110	24	66	64	42	1.6	6.6
no cat. /dark	110	24	3	3	0.09	0.07	0.3
Co_3O_4 -350-B*	110	8	>99	95	94	2.4	29.7
Co_3O_4 -350-B**	110	8	54	98	53	1.3	16.3
No cat/light	110	24	2	2	0.04	0.05	0.2

Reaction conditions - 10 mg Co_3O_4-350-B, 1 mL toluene, 25 - 110°C, 8-24 hours, ambient light, dark - covered with aluminum foil, 0.1 mmol benzylamine, 4 mL PTFE capped sealed glass vessels, TON - moles of benzylamine converted per mole of catalyst, TOF - moles of benzylamine converted per mole of catalyst per hour. Diphenylmethane was used as an internal standard to determine the GCMS standard error. (no cat. - no catalyst, * circular visible light reactor with 8W 16 light bulbs), ** circular UV light reactor with 8W 16 light bulbs

Since cobalt oxide demonstrated three photoexcitation regions (**Figure 5**a), the effect of visible light on the benzylamine coupling reaction was evaluated as shown in **Table 4**. Insignificant product yields (<0.3%) were noticed when either the temperature (110°C) or the catalyst was absent. Moderate (42%) yield was noticed under dark conditions (covered with aluminum foil) at 110°C with the catalyst. The highest homo-coupled product yield (>94%) was observed when the reaction was done in the visible-light photoreactor. The reaction was completed even within 8-12 h under visible photoexcited conditions. When the reaction was carried out under UV light irradiation as shown in **Table 4**, the homo-coupled product yield decreased to 53% (8h). In order to check whether the leached homogenous metal ions are responsible for the reaction, a leaching

test was performed. The solid catalyst was completely filtered out after 10 h of reaction using a 0.45 μm PTFE filter and the reaction was continued for another 14 h. Aliquots of the reaction solution were withdrawn every 5-hour intervals and GCMS analysis was performed. The reaction conversion was not changed after removing the catalyst from the reaction solution as shown in **Figure S15**.

In order to further improve the benzylamine coupling reaction and investigate the mechanistic details, transition metal ions (10% w/w) and graphene were "incorporated" on cobalt oxide during the cobalt oxide synthesis. These catalysts were calcined at 250°C and 350°C and used in the homocoupling reaction. X-ray diffraction patterns of ion/graphene incorporated cobalt oxide calcined at 250°C can be found in **Figure S16**. All peaks corresponding to bare cobalt oxide can be identified along with few additional diffraction peaks. Different morphologies (compared to bare cobalt oxide) were observed in the SEM images when different transition metal ions and graphene were incorporated on cobalt oxides as shown in **Figure S17**. Homogenous distribution of metal ions was noticed in the SEM/EDX elemental distribution analysis (**Figure S18**).

Homo-coupled product yields were significantly increased (compared to Co_3O_4-250-B 44%) when ion-incorporated, 250°C calcined samples (except Mo-Co_3O_4-250-B, 33%) were used as shown in **Table S9**. However, homo-coupled product yields were decreased (compared to Co_3O_4-350, 91%) when "incorporated" 350°C calcined samples were used as depicted in **Table 5.** The homo-coupled product yields were decreased in the order of Mn> Cu> graphene> Pd> Ni> Zn> Mo (250°C calcined samples) and Cu> Pd> Mn> Zn>Ni (350°C calcined samples) incorporation (**Figure S9**, **Figure 5**). Selectivities towards benzaldehyde (10%) and α-nitrotoluene (25%) were increased when Ni-Co_3O_4-250-B was used. However, above catalytic activity of nickel was inhibited (19% homo-coupled yield and no benzaldehyde or benzonitrile) when the catalyst was calcined at 350°C. Benzaldehyde (14%) and benzonitrile (26%) were detected when the Mn-Co_3O_4-350-B was used as the catalyst. A similar result was observed with the graphene-cobalt oxide (G-Co_3O_4-350-B) with 18% benzaldehyde and 25% benzonitrile selectivity. The selectivity towards benzonitrile was increased from 5% to 18% when the calcination temperature of Pd incorporated Co_3O_4 was increased from 250°C to 350°C.

Table 5. Effect of transition metal ion incorporated cobalt oxide calcined at 350°C on homo-coupling of benzylamine

Catalyst	**Conversion (%)**	**Selectivity (%) (a1)**	**Selectivity (%) (other)**	**Yield (%) (a1)**	**TON**	**TOF×10^{-2} (h^{-1})**
Cu-Co_3O_4-350-B	98	84	2(c)	82	2.4	9.9
Mn-Co_3O_4-350-B	>99	60	14(b), 26(c)	59	2.4	9.8
Zn-Co_3O_4-350-B	30	>99	NSP	30	2.4	9.9
Ni-Co_3O_4-350-B	19	>99	NSP	19	0.7	3.0
Pd-Co_3O_4-350-B	>99	72	18(c)	71	0.5	1.9
Mo-Co_3O_4-350-B	12	>99	NSP	12	2.4	9.9
Graphene-350-B	>99	56	18(b), 25(c)	55	0.3	1.2

Reaction conditions - 10 mg catalyst, 1 mL toluene, 110°C, 24 hours, ambient light, 0.1 mmol benzylamine, 4 mL PTFE capped sealed glass vessels, TON - moles of benzylamine converted per mole of catalyst, TOF - moles of benzylamine converted per mole of catalyst per hour. Diphenylmethane was used as an internal standard to determine the GCMS standard error. G-graphene. Selectivity a-coupled product, b-benzaldehyde, c- benzonitrile, d- α-nitrotoluene, NSP - no secondary products

3. Tandem amine homocoupling and amine-alcohol cross coupling

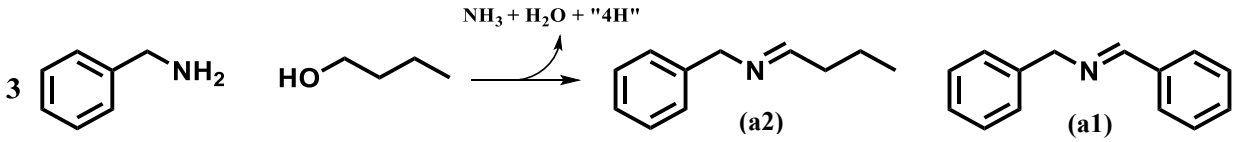

Figure 10. Tandem one-pot benzylamine homo-coupling (a1) and cross-coupling (a2) reaction

Benzylamine cross-coupling (CC) with alcohol (butanol) was observed when toluene was replaced with butanol. Two major products, homo-coupled, and CC products were observed as shown in **Figure 10.** Since alcohol oxidation normally requires a strong oxidant, transition metal ion incorporated (~10% w/w) cobalt oxide catalysts calcined at two different temperatures (250°C, 350°C) were first tested on homo and cross coupling reactions as shown in **Table 6 and S10**. The maximum yield of 39% CC product was observed when Mn-Co_3O_4-250-B (only 250°C calcined catalyst showing higher selectivity toward CC product than the homo-coupled product) was used whereas Co_3O_4-250/350-B showed 15% of CC product yield. Unlike 250°C calcined samples, higher CC product yields than homo-coupled products yields were observed with Cu-Co_3O_4-350-B (46%), Mn-Co_3O_4-350-B (36%), G-Co_3O_4-350-B (37%) catalysts. Both homo-coupling and cross-coupling reaction inhibition (4% and 2% yield respectively) was observed in the presence of Zn-Co_3O_4-250-B. Reaction inhibition by Zn was lifted at higher catalyst calcination temperatures (350°C). Higher benzylamine conversions were noticed when 350°C calcined samples (except Mo-Co_3O_4-350-B, 7% conversion) were used in the reactions instead of 250°C samples. Unlike Pd-Co_3O_4-250-B catalyst which resulted in homo and cross coupled products, Pd- Co_3O_4-350-B yielded tetrabutylammonium, butyl benzoate, and a derivative of homo-coupled product.

Even though Cu-Co_3O_4-350-B, Mn-Co_3O_4-350-B, G-Co_3O_4-350-B, and Mn-Co_3O_4-250-B seem to be good candidates for the tandem one-pot cross-coupled and homo-coupled product synthesis, reaction conditions were optimized with simple Co_3O_4-350-B catalyst to understand parameters involve in the reaction. Reaction time, temperature, alcohol-amine molar ratio, amine-alcohol substrate scope, and reaction environment were optimized as discussed in the following section.

Table 6. Effect of transition metal ion incorporated cobalt oxide calcined at 350°C on benzylamine homo-coupling and cross-coupling reaction with transition metal ion incorporated cobalt oxide calcined at 350°C

Catalyst	**Conversion (%)**	**Selectivity (%) (a2)**	**Selectivity (%) (a1)**	**Yield (%) (a2)**	**Yield (%) (a1)**	**(a) TON**	**(a) TOF×10^{-2} (h^{-1})**
Co_3O_4-350-B	>99	15	74	15	73	2.4	10.0
Cu-Co_3O_4-350-B	62	69	16	43	10	1.5	6.3
Mn-Co_3O_4-350-B	71	51	21	36	15	1.7	7.1
Zn-Co_3O_4-350-B	60	38	53	23	32	1.4	5.8
Ni-Co_3O_4-350-B	91	20	77	18	70	2.2	9.2
Mo-Co_3O_4-350-B	7	NPS	>99	NPS	7	0.2	0.8
G-Co_3O_4-350-B	68	54	29	37	20	1.6	6.7

Catalyst	Conv.	(e) Sel.	(f) Sel.	(g) Sel.	(e)Yield (%)	(f) Yield (%)	(g) Yield (%)
Pd-Co_3O_4-350-B	>99	19	45	28	19	46	28

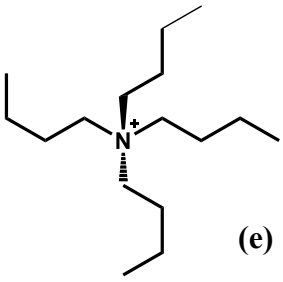

(e)

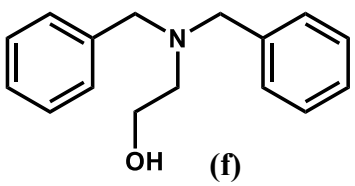

(f)

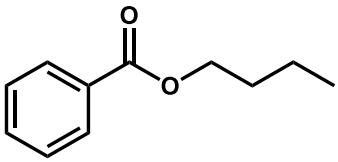

(g)

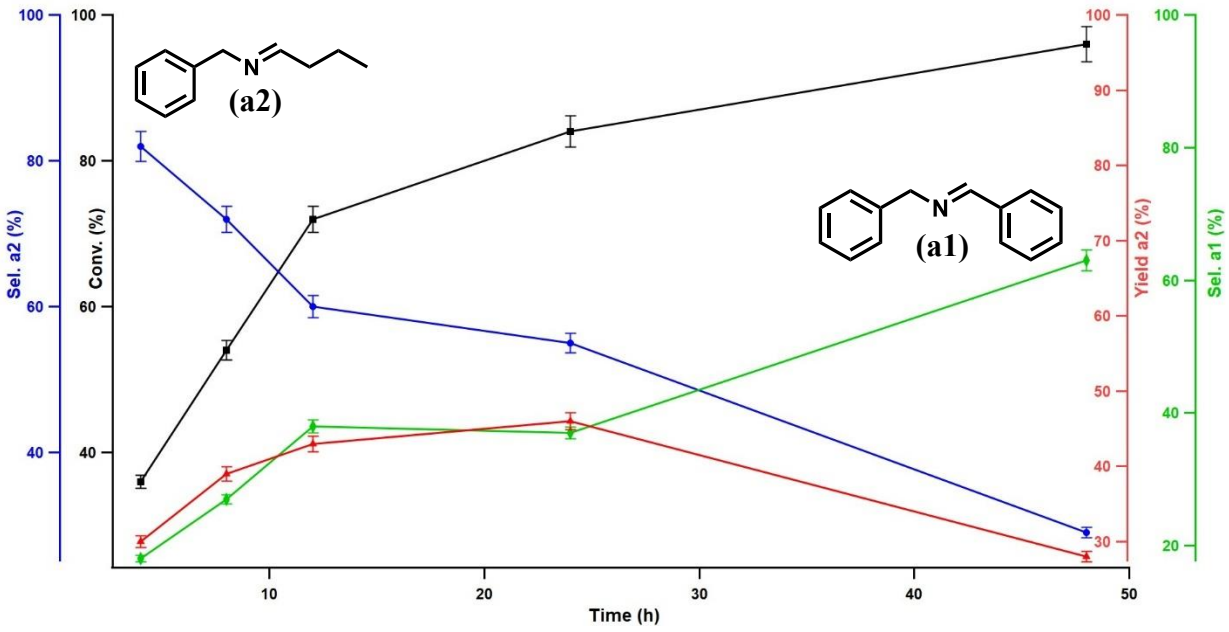

Figure 11. Change in the conversion, homo-coupling and cross-coupling selectivities, and CC yield over the reaction time. Reaction conditions (10 mg catalyst Co_3O_4-350-B), 1 mL butanol, 110°C, x hours, ambient light, 0.1 mmol benzylamine, 4 mL PTFE capped sealed glass vessels, TON - moles of benzylamine converted per mole of catalyst, TOF - moles of benzylamine converted per mole of catalyst per hour. Diphenylmethane was used as an internal standard to determine the GCMS standard error. Sel. - selectivity, conv. - conversion.

The reaction time was changed from 4-48 h and conversion, selectivities, and yield were calculated as shown in **Figure 11**. The CC product (a2) selectivities were more prominent (~80-60%) than homo-coupled (a1) product selectivity (~20-40%) until around 12 h. A steep, linear decrease in the CC selectivity and rapid linear increase in the homo-coupled product selectivity were identified during the first 12 h along with the linear increase in the conversion. Hence the 12 h reaction window was used in the reaction kinetic determination. As the rate of benzylamine conversion was started to decrease after 12 h, the CC product selectivity (or yield) continued to drop while homo-coupled product selectivity (or yield) continued to increase.

Products yields were recorded with respect to reaction temperature as shown in **Figure 12**. The reaction time was deliberately decreased to 8 h to get comparable data. Continuous increase in the benzylamine conversion was noticed until 110°C followed by a plateau at higher temperatures. Similar trend was observed in the homo and cross-coupled product yields until 100°C followed by an increase in the cross-coupled yield and decrease in the CC yield at 130°C.

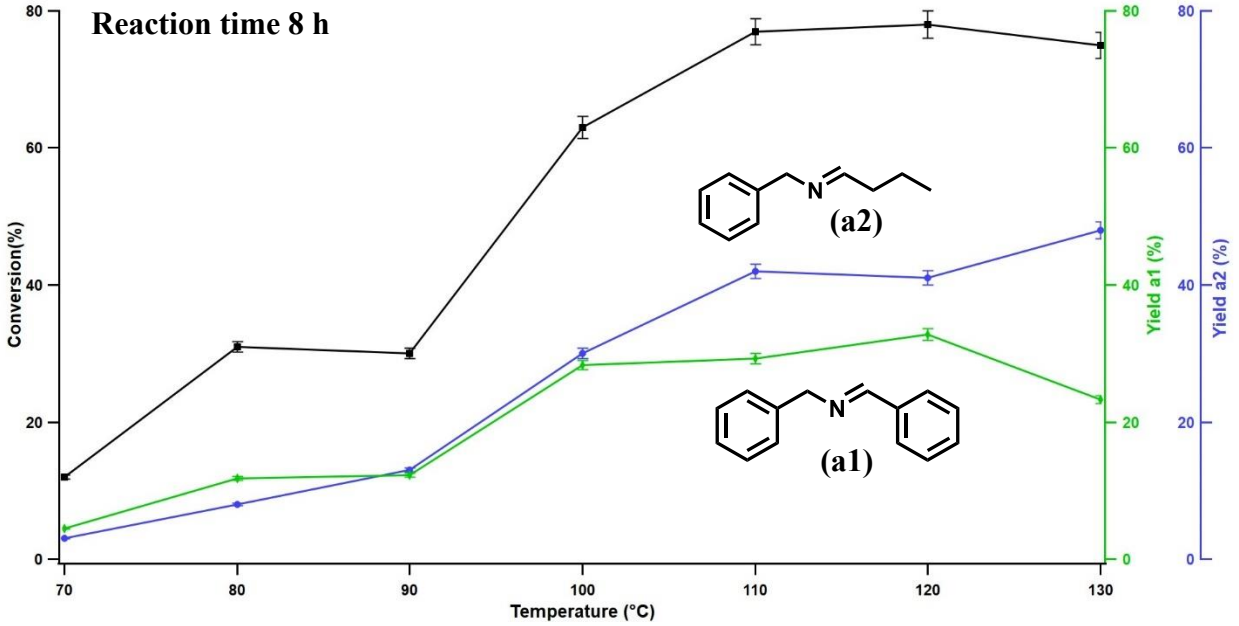

Figure 12. Change in the benzylamine conversion and product yields (a1 and a2) with respect to the reaction temperature.

Reaction conditions (10 mg catalyst Co_3O_4-350-B), 1 mL butanol, X°C, 8 hours, ambient light, 0.1 mmol benzylamine, 4 mL PTFE capped sealed glass vessels, TON - moles of benzylamine converted per mole of catalyst, TOF - moles of benzylamine converted per mole of catalyst per hour. Diphenylmethane was used as an internal standard to determine the GCMS standard error.

The volume of the butanol was increased from 2 mL to 10 mL to suppress the active site-benzylamine interactions and to improve the alcohol oxidation reaction. The lowest CC product selectivities were observed at higher or lower (2 mL or 10 mL) butanol volumes while constant selectivity values around 20% were noticed at moderate butanol volumes as shown in **Figure 13**. A decrease in the benzaldehyde selectivity was noted as the butanol volume increased from 2 mL to 10 mL. The increase in the reactor vessel volume (2.5 mL to 25 mL) should be considered when comparing the data to other experiments.

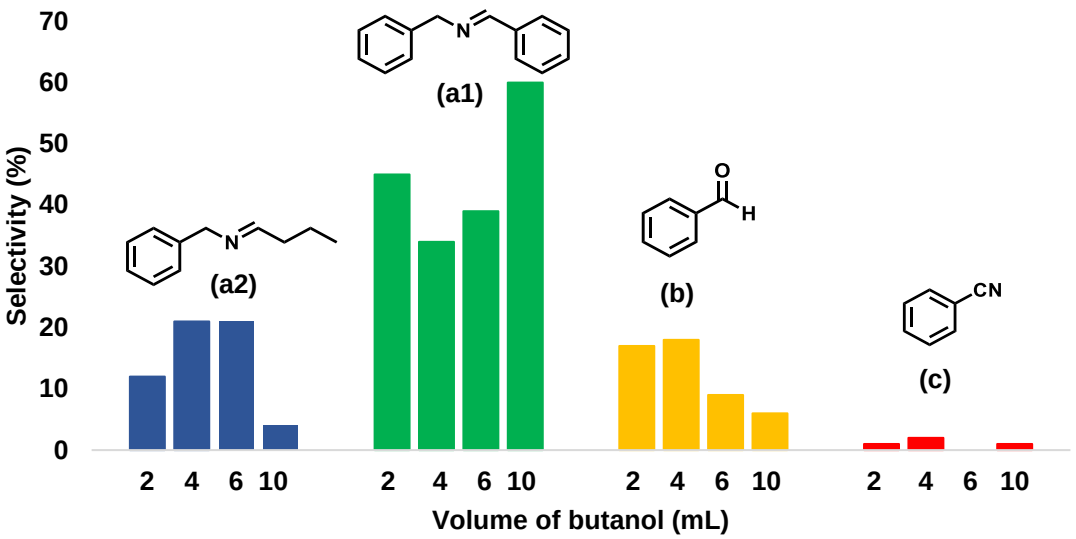

Figure 13. Change in the products selectivities with respect to the butanol volume

Reaction conditions (10 mg catalyst Co_3O_4-350-B), V mL butanol, 110°C, 24 hours, ambient light, 0.1 mmol benzylamine, 25 mL PTFE capped sealed glass vessels, TON - moles of benzylamine converted per mole of catalyst, TOF - moles of benzylamine converted per mole of catalyst per hour. Diphenylmethane was used as an internal standard to determine the GCMS standard error.

Table 7. Alcohol substrate scope in benzylamine coupling reactions

Solvent	Conversion (%)	Selectivity (%) (a2)	Selectivity (%) (a1)	Yield (%) (a2)	TON	TOF×10^{-2} (h^{-1})
Methanol*	36	82	13	30	0.9	1.5
Ethanol*	80	66	17	53	1.9	3.3
1-Propanol*	67	31	58	21	1.6	6.7
1-Butanol	67	44	37	29	1.6	6.7
1-Pentanol	72	40	56	29	1.7	3.0
1-Hexanol	72	42	26	30	1.7	3.0
1-Heptanol	>99	29	35	25	2.4	10.0
1-Nonanol	84	NPS	>99	NPS	2.0	8.3
Cyclohexylmethanol	>99	43	56	43	2.4	10.0

Reaction conditions (10 mg catalyst Co_3O_4-350-B), 1 mL alcohol, 110°C, 24 hours, ambient light, 0.1 mmol benzylamine, 4 mL PTFE capped sealed glass vessel, * 25 mL stainless-steel high-pressure reactor. TON - moles of benzylamine converted per mole of catalyst, TOF - moles of benzylamine converted per mole of catalyst per hour. Diphenylmethane was used as an internal standard to determine the GCMS standard error. NPS – no product selectivity

Butanol was replaced with a series of aliphatic alcohols as depicted in **Table 7** to check the substrate scope of the reaction. The first three reactions were done in a high-pressure reactor due to lower boiling point (<100°C) compounds. A general increase in the benzylamine conversions (except in the case of ethanol) was observed with the increase in alcohol carbon number. Benzylamine conversions around 67%-72% were noticed with C3-C6 alcohols and a maximum conversion (>99%) was observed with C7 alcohols. The decrease in the conversion down to 84% was seen when the carbon number was increased to 9. A general decrease in the CC selectivity

and increase in the homo-coupled product selectivity were observed with the increase of alcohol carbon number.

Table 8. Amine substrate scope in butanol-amine cross coupling reactions

Amine	**Conversion (%)**	**Selectivity (%)**	**Yield (%)**	**TON (a)**	**TOF×10^{-2} (h^{-1})**
$C_6H_5CH(CH_3)NH_2$	40	88(i)	35(i)	1.0	4.2
Aniline	59	94(j)	55(j)	1.4	5.8
n-Butylamine	>99	94(k)	93(k)	2.4	1.0
Cyclohexylamine	80	89(l)	71(l)	1.9	7.9
Hexylamine	>99	30(m)	30(m)	2.4	10.0

Reaction conditions (10 mg catalyst Co_3O_4-350-B), 1 mL butanol, 110°C, 24 hours, ambient light, 0.1 mmol amine, 4 mL PTFE capped sealed glass vessels, TON - moles of benzylamine converted per mole of catalyst, TOF - moles of benzylamine converted per mole of catalyst per hour. Diphenylmethane was used as an internal standard to determine the GCMS standard error.

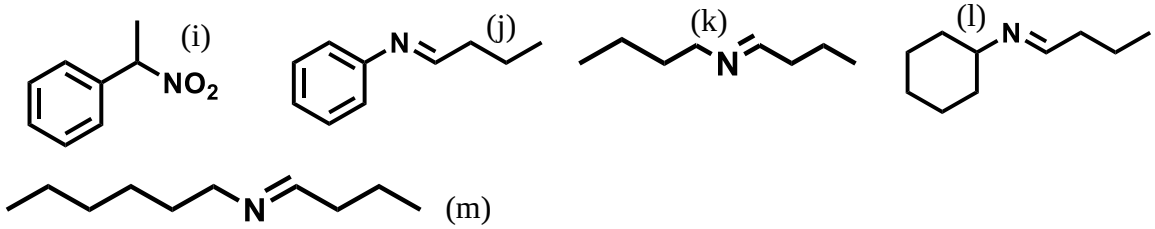

Benzylamine was replaced with a series of amines while keeping butanol amount constant as shown in **Table 8** to check the substrate scope of the reaction. Oxidized product, 1-nitroethylbenzene, was observed instead of the homo-coupled product when 1-phenylethylamine was used as the amine. Lower conversions (<60%) were noted with both aromatic amines (aniline, 1-phenylethylamine) whereas aliphatic amines resulted in higher conversions (>80%). Nearly 90% selectivity for butanol-amine cross coupling products was observed except in the case of hexylamine (30%). Butanol to benzylamine molar ratio was changed and the homo-coupled product yields were recorded with respect to time as shown in **Figure S18**. Almost similar product yields were observed up to 12 hours irrespective of the molar ratios between butanol to

benzylamine. The recyclability of the catalyst was tested as depicted in **Figure S22** and no significant decrease in the activity was noticed even after 5 cycles. Calcination of the sample after 5^{th} cycle resulted in about a 6% increase in the conversion.

4. Understanding the reaction mechanism

Table 9. Effect of the reaction environment on the selectivity of the reaction

Reaction environment	Conversion (%)	Selectivity (%) (a2)	Selectivity (%) (a1)	Yield (%) (a1)	TON	TOF×10^{-2} (h^{-1})
Helium	71	2	98	70	1.7	7.1
Oxygen	97	1	88	85	2.3	9.6
Carbon dioxide	54	4	92	50	1.3	5.4
Ammonia	59	3	76	45	1.8	7.5

Reaction conditions (10 mg catalyst Co_3O_4-350-B), 1 mL butanol, 110°C, 24 hours, ambient light, 0.1 mmol benzylamine, Top end sealed reflux system with 25 mL round bottom flask , gas balloon, TON - moles of benzylamine converted per mole of catalyst, TOF - moles of benzylamine converted per mole of catalyst per hour. Diphenylmethane was used as an internal standard to determine the GCMS standard error. * Reaction environment was established by vacuum and gas purge cycles. The pH of the product solutions was pH ~ 6 (CO_2) and 8 (NH_3) at the end of the reaction.

The reactions were conducted under different atmospheres; vacuum, oxygen, acidic, basic, to understand the reaction mechanism as shown in **Table 9**. A 28% suppression in the benzylamine conversion was noticed under non-oxidative (helium, 71%) conditions compared to the oxidative atmosphere (pure oxygen, 97%). Further suppression in the conversions was observed when the atmosphere was changed to ammonia (59%) and carbon dioxide (54%). Insignificant (<2%) CC product selectivity was observed in all four scenarios. The difference in reactor types (sealed small volume reactor vs sealed large volume reflux) should be noted when comparing the data.

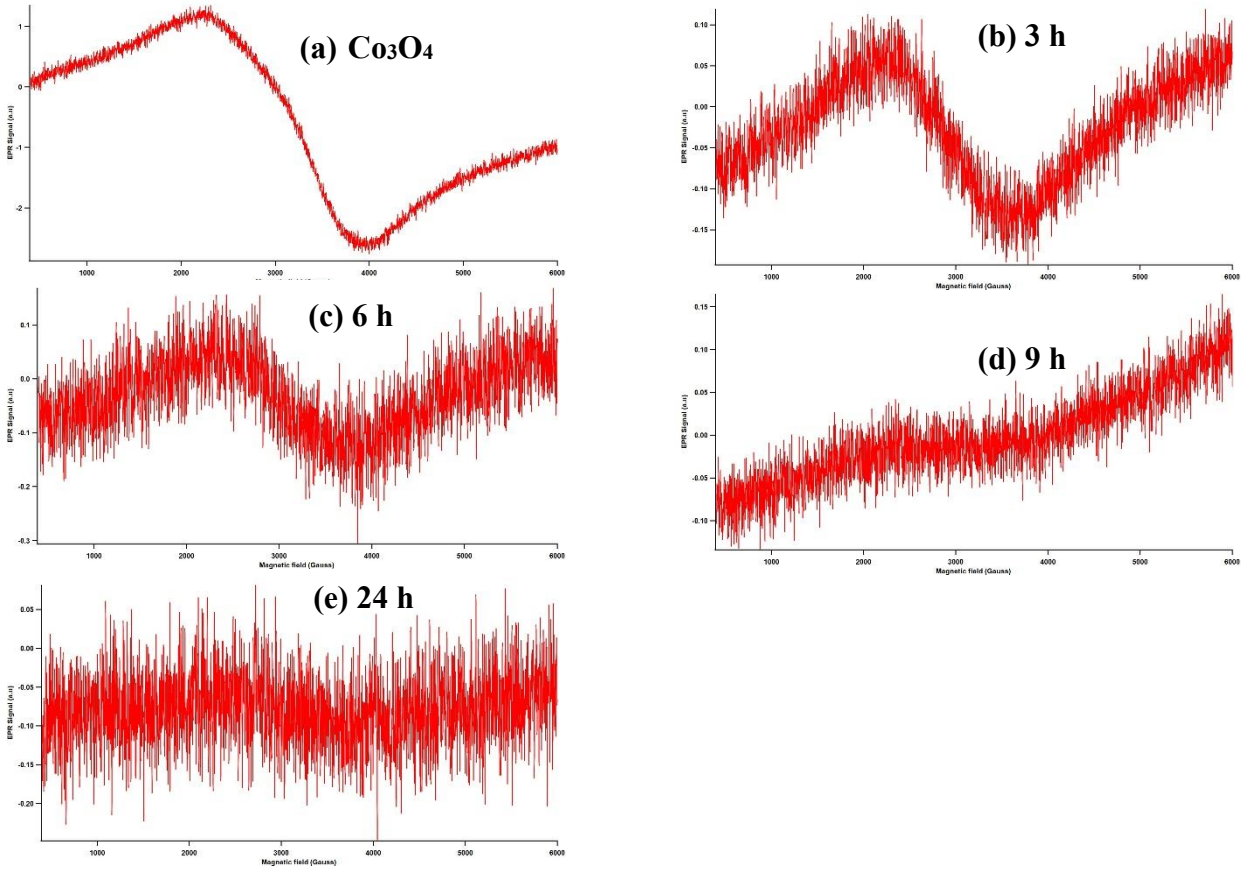

Figure 14. *In situ* EPR spectra of benzylamine homo-coupling reaction. EPR signal of Co_3O_4-B-350 powder (a) in air: in toluene after (b) 3 h (c) 6 h (d) 9 h (e) 24 h of reaction time. Reaction conditions - 10 mg catalyst, 110˚C, 0.1 mmol benzylamine in a caped EPR tube

An *In situ* EPR study was done in order to understand the redox activity of the catalyst and the role of spinel cobalt oxide in the reaction. A broad EPR signal was observed when cobalt oxide powder was packed in the EPR tube as shown in Figure 14a. EPR signal to noise ratio was increased when the catalyst was dispersed in toluene and heated at 110°C for 3 hours as depicted in Figure 14b. A decrease in the EPR signal intensity was noticed as the benzylamine homo-coupling reaction progressed for 24 h.

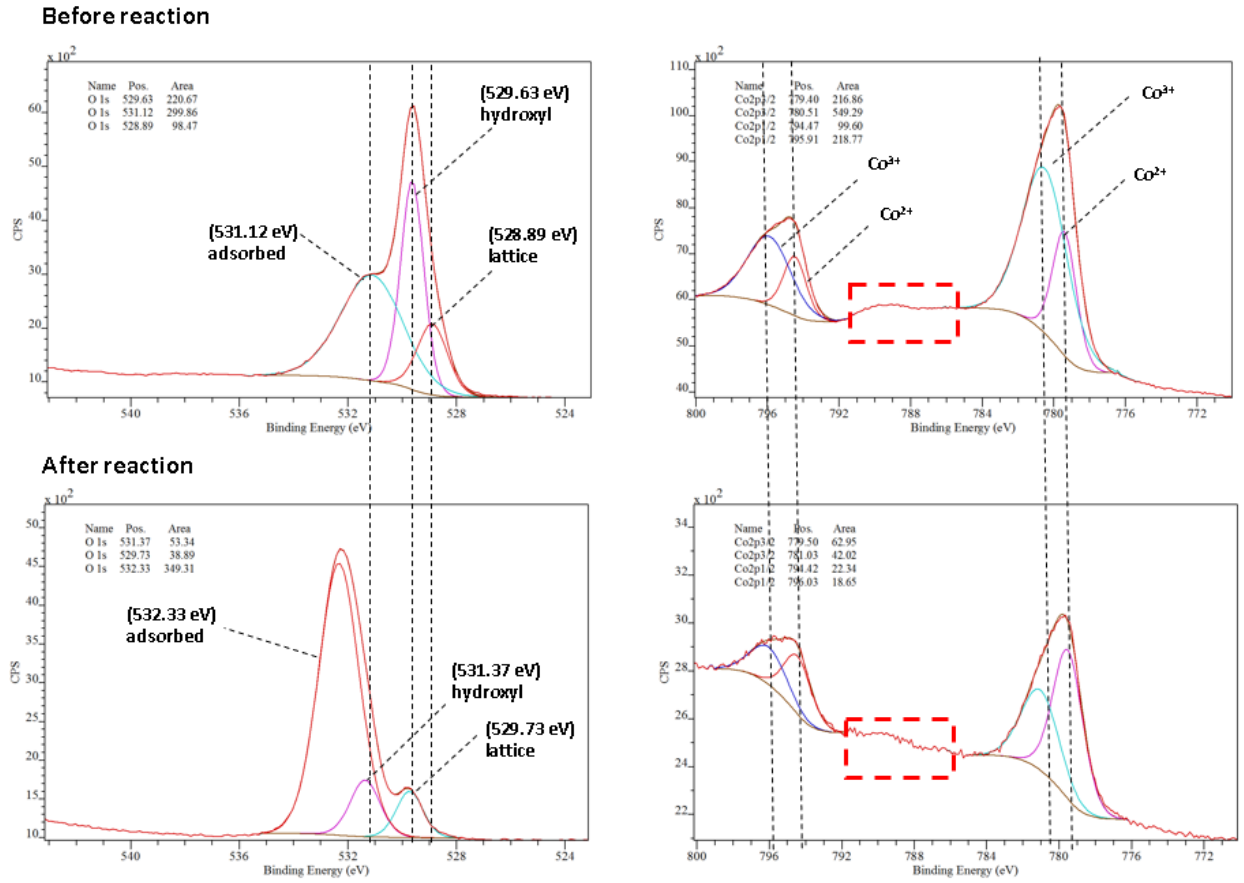

Figure 15. XPS spectra of cobalt oxide (Co_3O_4-B-350) pre and post benzylamine coupling reaction

The observation in the EPR study was further supported by XPS analyses of fresh and used cobalt oxide catalyst as shown in **Figure 15**. Three deconvoluted peaks were fitted inside the oxygen 1s area and two peaks were fitted inside each Co 2p area. Changes in XPS peak areas, peak positions, and shapes were recognized when fresh and used catalysts were compared. Peak positions were shifted to higher binding energy in the used catalyst compared to fresh catalyst. The area of the deconvoluted peak at 779.40-779.50 eV was increased compared to the area of the deconvoluted peal at 780.5-781.0 eV in the used catalyst.

Table 10. Reactive oxygen species scavenger test for benzylamine coupling reaction

Reactive oxygen species (ROS) scavenger	ROS	Conversion (%)	Selectivity (%) (a2)	Selectivity (%) (a1)	Yield (%) (a2)	Yield (%) (a1)	TON	TOF×10^{-2} (h^{-1})
None	None	71	62	34	44	24	1.7	7.1
Ammonium oxalate	Holes	22	58	40	13	9	0.5	2.1
tert-butyl alcohol	OH radical	73	59	33	43	24	1.8	7.5
TEMPO	Radicals	86	52	40	45	39	2.1	8.8
Sodium azide	Singlet oxygen	>99	87	8	87	8	2.4	10.0
Mannitol	OH radical	59	6	85	4	50	1.4	5.8

Reaction conditions (10 mg catalyst Co_3O_4-350-B), 1 mL butanol, 110°C, 24 hours, ambient light, 0.1 mmol amine, 2 mg ROS scavenger, 4 mL PTFE capped sealed glass vessels, TON - moles of benzylamine converted per mole of catalyst, TOF - moles of benzylamine converted per mole of catalyst per hour. Diphenylmethane was used as an internal standard to determine the GCMS standard error.

Reactive oxygen species (ROS) participating in the reaction were recognized by the ROS scavenger test as shown in **Table 10**. Ammonium oxalate, tert-butyl alcohol, (2,2,6,6-tetramethylpiperidin-1-yl)oxidanyl (TEMPO), sodium azide, were used to scavenge *in situ* generated holes, hydroxyl radicals, superoxide radicals, singlet oxygen respectively. Mannitol was used as a secondary hydroxyl radical scavenger due to the low boiling point of tertbutyl alcohol. Benzylamine conversion was dropped down to 22% from 71% in the presence of the hole scavenger. All other scavengers, except mannitol, resulted in similar or even higher conversion

than the blank experiment. Even though the conversion reached >99% in the presence of singlet oxygen scavengers, the homo-coupled product yield dropped down to 8% and CC product yield reached 87%. A decrease in the cross-coupled product yield (4%) was observed when hydroxyl radical scavenger, mannitol was used. Decrease in the conversion (22%) was observed when hole scavenger was utilized in the reaction.

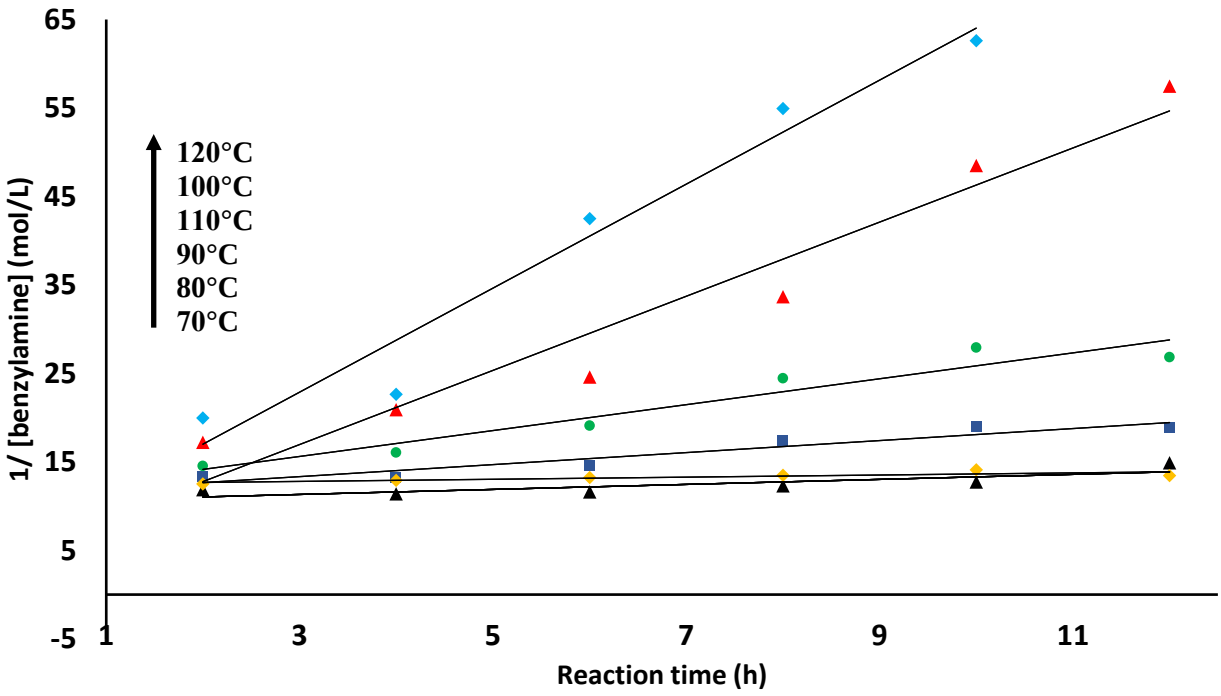

Figure 16. Second order kinetic plots for benzylamine coupling reaction at different temperatures Reaction conditions (10 mg catalyst Co_3O_4-350-B), 1 mL butanol, X°C, Y hours, 0.1 mmol amine, 4 mL PTFE capped sealed glass vessels, TON - moles of benzylamine converted per mole of catalyst, TOF - moles of benzylamine converted per mole of catalyst per hour. Diphenylmethane was used as an internal standard to determine the GCMS standard error.

Integrated rate law equation (zeroth, first, second, etc.) plots were constructed by considering the remaining amount of benzylamine during the course of the reaction as depicted in **Figure 16, S20, and S21**. The coefficients of determination (COD) of each reaction order at each temperature were summarized as shown in **Table S11**. The Arrhenius plots (second order **Figure 17**) were constructed for all three kinetic orders and reaction activation energies were calculated to get an idea about the kinetics of the reaction. The activation energies of the reaction increased with the used kinetic-order in the order of zeroth, first and second. Even though COD values are almost

similar in zeroth, first, and second order models, second order reaction kinetic was predicted considering the activation energy of the second order reaction

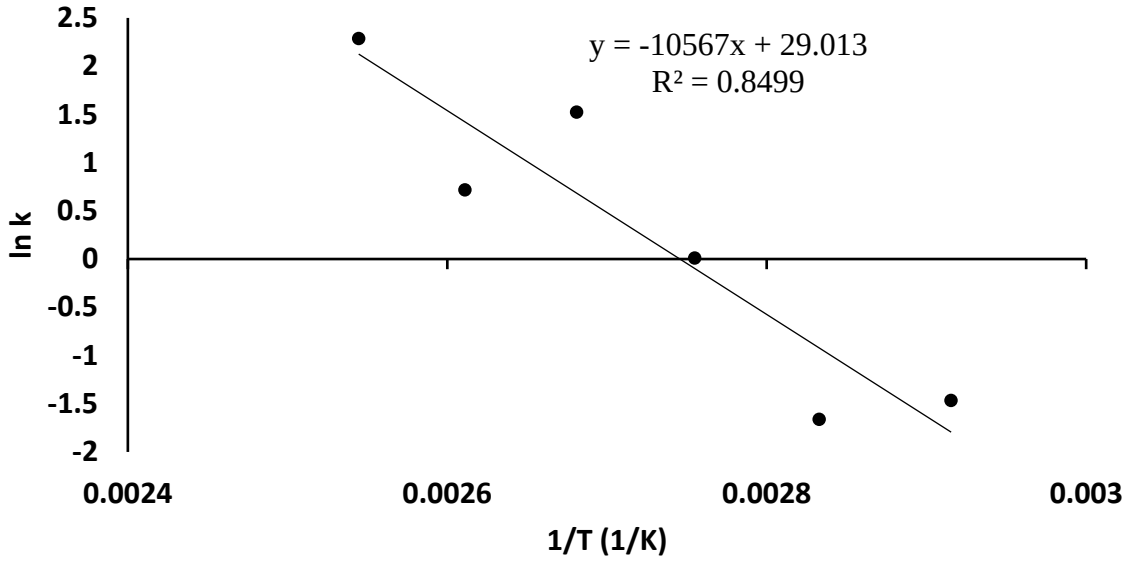

Figure 17. Arrhenius plot for benzylamine coupling reaction considering second order reaction kinetics

Discussion

1. Material Characterization

Surfactants have been extensively used in the synthesis of ordered mesoporous silica, carbon, metal oxides, phosphates in the literature.[27] Effects of nonionic, ionic (cationic, anionic), and amphoteric surfactants in controlling crystallite sizes and pore size distributions have been investigated in different studies.[28,29] Six different nonionic surfactants (**Figure S1**) in the categories of PEO-PPO-PEO triblock copolymer (A; Synperonic F108, P123), Sorbitan esters (B; Span 80, C; Tween 80), oligomeric alkyl PEO (D; Birj 58), and E; PEG-400 were used in this study to synthesize mesoporous cobalt oxide. Different crystallite sizes, shapes, particle morphologies, lattice strains, gas sorption related parameters, optical band gaps, and chemical environments were demonstrated by catalysts prepared with above six surfactants (A-E and P123) having different molecular weights, B; Span 80 (428 $gmol^{-1}$), E; PEG 400 (380-420 $gmol^{-1}$), F; P123 (5800 $gmol^{-1}$), A; F108 (14600 $gmol^{-1}$), C; Tween 800 (1310 $gmol^{-1}$), D; Birj 58 (79000).

Relationship between physiochemical properties of above cobalt oxide catalysts and their catalytic activity on amine-alcohol/amine-amine coupling reactions was investigated in the current study.

The profile broadening (full width at half maximum, FWHM) in the XRD patterns can be described in terms of crystallite sizes and micro-strains (due to compressive and tensile forces) according to the HW equation (**Figure S2-S7**). Imperfections in the crystallites such as dislocations, grain boundaries form during the *in-situ* crystallite growth process are responsible for the micro-strains.[30] Nanoparticle sintering/agglomeration is considered as the main factor responsible for the crystallite size deviation. Therefore, the discrepancies in FWHM observed in six samples can be attributed to surfactant mediated lattice defects generation or/and sintering variations. Differences in the crystallite sizes (**Figure S8**) predicted by the Scherrer and HW equations can be attributed to the assumptions made during the equation derivations (shape factor, etc.). The Halder-Wagner (HW) method is considered as an appropriate model to determine micro-strains (**Figure S9)** and sizes since the HW model utilizes more reliable regions of 2 theta values than the WH method during calculations.

Curved reverse micelles can be formed by triblock (apolar-polar-apolar units) copolymer surfactants (A and P123) in butanol (dielectric constant 17.5) whereas simple reverse micelles could be formed by surfactant B, C, D.[26,31] Micelle structures cannot be expected from the surfactant E due to the short chain hydrophilic nature. Compartmentalization of oxo-metal clusters by surfactant chains and interactions between surfactants and metal cluster surfaces govern the crystallite growth occur via sintering process. Bulky polar heads containing surfactants (B, C) tend to stabilize small nanoparticles and prevent nanoparticles agglomeration whereas triblock copolymers (A, P123) lead to largest crystallite sizes due to the presence of spacious curved micelle pockets which can accommodate higher number of nanoclusters. Larger crystallites formation as the calcination temperature increases from 250°C to 350°C (**Table S1**) can be attributed to sintering of particles. Generally, smaller crystallite with high surface area densify much faster than larger crystallites. The different degrees of slow CO_3O_4 crystallites sintering can be attributed to the surfactant stabilization of nanoclusters. Insignificant strain values in A-250 and B-250 could be attributed to insignificant lattice defects in the nanostructure. Decrease in the strains (i.e. defects) of samples C and D and increase in the strains of samples E and F with the

increase in the calcination temperature can be interpreted in term of changes in defects sites during the sintering.

Crystallite morphology of a catalyst is an important factor which determines the catalytic activity.[14] Catalysts prepared with Span 80 (B) and Birj 58 (D) have a unique rod-shaped morphology which can be identified in the TEM images (**Figure 2c, g**). These rods were composed of spherical nano-crystallite building blocks (9-20 nm) as shown in **Figure 2b, 2d, 2e**. These elongated rods can be further arranged into the spherical microparticles as seen in the SEM image (**Figure 3**). Since the sample preparation in TEM uses a sonication technique, these microspheres can be resolved into their elongated rods or spherical nano-crystallites during the sonication. The regularity of crystallites surfaces (steps) is another important factor responsible for the kinetics of a catalytic reaction. According to the surface depth variation profile (**Figure 2h-k**) of six samples, sample B has the most regular surface. The particle sizes determined from the XRD were reconfirmed by analyzing the particle sizes under TEM (**Table S1**). Peak positions and intensities observed in XRD patterns were reconfirmed by the selective area electron diffraction (SAED) patterns. The semi-continuous nature of SAED rings (**Figure S10**) can be attributed to borderline polycrystalline to single crystal nature of the particles. Differences in the particle morphologies and sizes observed under SEM could be attributed to differences in the surfactant chemistry. Surfactants B, C, and D have sixteen carbon hydrophobic tails and hydrophilic heads. However, surfactant C is different from B and D due to that fact that surfactant C has a bulky hydrophilic head. Surfactant A, E, and P123 have a recurring hydrophilic ether active group and small hydrophobic methyl groups.

According to the IUPAC classification of mesoporous materials explained by Thomas et al.[32], samples A-E and P123 resembled type IV(a) isotherm (**Figure 4**) which indicates mesoporous nature of a materials. The H1 type nitrogen adsorption-desorption hysteresis curves suggest either well-ordered cylindrical channels or spherical pores in the materials. Lack of low-pressure hysteresis can be explained by rigid pores which do not expand or shrink depending on the gas absorption and desorption.[32] The hysteresis in the type IV isotherm of nitrogen adsorption-desorption curve is a good indication of mesopores having width larger than 4 nm.[33] Similar and smaller pore diameters (9.6 nm) can be correlated to bulky polar head surfactants (B and C) whereas larger pore diameters (17.4 nm and 12.4 nm) could be formed due to triblock copolymers,

A and P123, which can arrange into curved surfactant chains (**Table 1**). Lowest surface area (33 m^2/g) and pore dimensions (7.8 nm) of sample E-350 can be explained by the incapability of surfactant t E to form inverse micelles in butanol. The higher pore diameter of D-350 (similar to A-350) and lower surface area (59 m^2/g) could be a result of straight chain surfactant without bulky polar heads. The above observations suggest that different surfactants can be utilized to fine tune the mesoporous pore diameters, volumes, and surface areas of a catalyst.

Spinel cobalt oxide (Co_3O_4) has cubic AB_2O_4 structure where Co^{2+} ions reside in tetrahedral sites and Co^{3+} ions occupy octahedral sites with 1:2 stoichiometric ratio.[34] The tetrahedral high spin Co^{2+} $[(e)^4(t_2)^3]$ possesses three unpaired electrons whereas all electrons in low spin octahedral $[(t_{2g})^6 (e_g)^0]$ Co^{3+} are paired. When these orbitals overlap with ligand (O 2p) orbitals, conduction (mainly composed of Co^{2+} t_2, Co^{3+} e_g) and valance (mainly composed Co^{2+} e, Co^{3+} t_{2g}, and O 2p) bands are formed. Three absorbance peaks (**Figure 5**) in the Kubelka-Munk diffuse reflectance spectra can be assigned to charge transfer processes (ligand to metal , metal to metal, and d-d transitions) which occur between aforementioned orbitals.[35] According to Orgel diagrams, d^6 (Co^{3+}) octahedral systems can only have one allowed d-d transition whereas d^7 (Co^{2+}) tetrahedral can have three allowed d-d transitions which typically occur in the range of 375 nm - 510 nm.[36] Therefore one can argue that the broad peak around 425 nm may correspond to the above d-d transitions. However, theoretical[37] and experimental studies[38,39] ambiguously assigned broad absorbance peaks centered at 425 nm and 723 nm to O^{2-} to $Co^{3+}(O_h)$ and/or O^{2-} to $Co^{2+}(T_d)$ ligand to metal charge transfers. The conduction (CB), valence (VB) band energy diagram **(Figure S11)** of Co_3O_4 was established with the help of XPS valence band (**Figure S12**) and UV-Visible absorbance edges. Even though almost similar UV-visible absorbance edges (**Table S2**) were noticed in all six cobalt oxide samples, differences in the valence band edge energies could have shifted the actual energies of the CBs (assuming XPS_{VB}+ UV-Vis $_{band\text{-}gap}$ = CB). If electronic excitations originate from valence bands with O^{2-} 2p characteristics, there should be four distinct energy levels above the VB to explain the four absorbance edges. Three low energy excitations with 1.5, 2.0, 2.2 eV can be explained by referring to the theoretical density of states diagram of Co_3O_4 reported by Singh et al.[37] The relatively high intense peak around 239 nm can be attributed to the ligand to higher energy metal orbital (higher than CB Co^{3+} 3d) charge transfer.

According to the group theory, Fd-3m space group can have five Raman active modes, $3F_{2g}$, $1E_g$,$1A_{1g}$.[40,41] Raman peaks (**Table S3**) at 185 cm^{-1}, 507 cm^{-1}, and 615 cm^{-1} can be attributed to $3F_{2g}$ whereas peaks at 466 cm^{-1}, 669 cm^{-1} can be assigned to E_g and A_{1g} respectively.[42] Peaks at 185 cm^{-1} and 669 cm^{-1} have been assigned to tetrahedral and octahedral sites respectively. The peak intensities of above two bands reflect the stoichiometry (1:2) of Co^{2+} and Co^{3+} in spinel Co_3O_4. Slight Raman peak shifts in six samples can be explained by optical phonon confinement phenomena which cause uncertainty in the wave vectors of the phonons.[43]

Six main regions can be identified in the high-resolution cobalt 2p XPS spectra (**Table S4**). Peaks at 779.3-780.1 eV (post 770.5 eV), 780.1-781.5 eV (post 781.0 eV), 794.0-795.2 eV (post 794.4 eV), and 795.4-796.8 eV (post 796.0 eV) can be attributed to $2p_{3/2}$ Co^{2+}, $2p_{3/2}$ Co^{3+}, $2p_{1/2}$ Co^{2+}, and $2p_{1/2}$ Co^{3+} respectively. The broad peak around 790 eV can be assigned to the satellite peak of the Co $2p_{3/2}$. Highest Co^{3+}/Co^{2+} ratio (2.7) was observed in the Co_3O_4-350-B and the lowest ratio (1.6) was noted for Co_3O_4-350-P123 (**Table S5**). Deviations from the ideal spinel cobalt oxide octahedral to tetrahedral sites ratio (2:1) on the surface can be attributed to lattice defects. Peaks (**Table S6**) at 529.6-529.5 eV in XPS O 1s high resolution spectra can be attributed to the lattice oxygen whereas peaks at 530.1-531.3 eV can be ascribed to surface hydroxyl groups. Surface adsorbed species such as water and oxygen typically show higher binding (>532 eV) energy than the other two.[44] Comparatively high intensity peak at 532.3 eV in the post-reaction sample (**Figure 15**) than fresh catalyst suggest adsorbed water (water generation during reaction) on the catalyst.[45] A decrease in the surface Co^{3+} ion density and increase in the Co^{2+} amount during the reaction suggest electron accepting behavior of the spinel cobalt oxide. A slight peak shift towards high binding energy in both hydroxyl and lattice oxygen of the post-reaction catalyst compared to the fresh catalyst suggest reduction in the electron density in oxygen species during the reaction (**Figure 15**).

The anodic peak around ~0.25 eV in CV can be assigned to the Co^{2+} oxidation to Co^{3+} species ($Co_3O_{4\,(s)} + OH^-_{(aq)} + H_2O_{(l)} \rightarrow 3\ CoOOH_{(s)} + e$) whereas the peak around 0.2 eV in the reduction branch can be attributed to the reverse reaction. Peaks corresponding to $Co^{3+} \leftrightarrow Co^{4+}$ were not observed in the used potential window.[46] The oxidation maximum peak positions shift to positive potentials (**Figure 8)** in the sequence of P123< D< B< E< C< A which suggests decreased electron density of Co^{3+} species along the sequence.[47] On the other hand, the maximum cathodic potentials

decreased in the order of D>A>C> B> P123> E. Sample B demonstrated moderate redox potentials compared to other five samples. Higher peak areas in samples C and E than other samples (D< A< B< P123< C< E) suggest higher capacitance.[48] Even though a clear pattern cannot be established between reactivity and redox capability of Co_3O_4, surfactant dependent changes in the electrochemical properties are evident.

2. Benzylamine homocoupling reaction

Correlation between crystallite size, surface area, pore volume, and catalytic activity of different catalysts has been established in various studies.[49–51] Effects of crystallite size, lattice strain, surface area, pore volume, chemical states, surface morphology, and bonding of cobalt oxide on benzylamine homocoupling reaction has been evaluated in the current study. The highest homo-coupled product yield in B-350 sample could be attributed to a combined effect of small crystallite size (13 nm), smooth rod-shaped crystallite surfaces, small particle size (<2.8 μm), high surface area (85 m^2/g), high Co^{3+}/Co^{2+} ratio (2.7), lowest VB band edge, and higher photo-absorption intensity. The product yields in E-350 and E-250 reactions could be limited by the low surface area (33 m^2/g), limited pore diameter (7.8 nm), low photo-absorbance, and lowest Co^{3+}/Co^{2+} ratio (1.8) of the catalyst. Since several *in situ* factors (mentioned above) are responsible for the catalytic activity, it is not practical to predict individual correlations. Drop in the product yields (except sample B) with the increase in the calcination temperature (250°C to 350°C) can be attributed to the crystallite sintering associated changes (**Table S1, Table 2, and Table S8**). Even though sample B also endured sintering, the catalytic activity was increased with the 350°C sintering (B; 250, 7 nm, 44% to 350, 13 nm, 90% and C; 250, 12 nm, 79% to 350, 17 nm,35%) which could be attributed to a gaussian like size-activity relationship.

The unique catalytic trend of the B-350 in different solvents (**Figure S14**) can be explained in terms of smaller crystallite size and high surface area. Higher catalytic activity in dimethylacetamide can be attributed to the presence of lone-pair nitrogen atoms which can facilitate the proton abstraction during dehydrogenation. Similar α-protons abstraction by nitrogen active sites of flavin adenine dinucleotide (FAD) of mammalian monoamine oxidase which catalyze amine to aldehyde conversion has been reported eralier.[52] Even though the catalytic activity in toluene was comparatively (dimethylacetamide) low, toluene was selected as the solvent of choice considering the reaction promotion by solvent, dimethylacetamide. Lower homo-coupled

product yields in the presence of cyclohexanone and 1-butanol solvents can be explained by secondary products including cyclohexanone-benzylamine and butanol-benzylamine cross-coupled product formation.

Insignificant or limited effect of substituents on the homo-coupling reaction has been reported in early studies.[53,54] Few significant trends have been recognized in the current study as mentioned in the result section (**Table 3**). Observation of the lowest homo-coupled product yields in the presence of ortho (o) or meta (m) substitution can be rationalized in terms of steric hindrance of o, m compared to para substitution. The above observation suggests that not only the amine binding sites are responsible for the reaction but also the surrounding sites (similar to the mammalian monoamine oxidase enzyme).[55] Explanation of the current reaction in terms of earlier reported (V_2O_5 catalyzed) benzylic anion mediated reaction mechanism[54] seems ambiguous since both electron donating (ED) or withdrawing (EW) substitution in this study has similar effect on homocoupling reaction. Dependability of imine formation rate on the magnitude of the partial positive charge of the carbonyl carbon (increase by EW, more α-H dehydrogenation) and base strength of the amine (increase by ED) further explain the results in **Table 3**.

The improvement of homocoupling reaction by photoexcitation of Co_3O_4-350 (**Table 4**) can be further supported by the singlet oxygen formation reported in **Table 10**. Increase in the homo-coupled product yield in the presence of visible light compared to UV light suggests participation of the 425 nm absorption edge of Co_3O_4 during the excitation process (**Table 4**). Promotion of the homocoupling product yield by Mn, Cu, Pd, Ni, and graphene based catalysts has been reported in the literature.[6] Product yield improvement by above metal ions incorporated cobalt oxide (**Table 5)** is consistent with the literature. Further studies are ongoing in order to understand the adverse effects of Ni, Zn, and Mo incorporation and calcination temperature on the homocoupling reaction.

3. Tandem amine homocoupling and amine-alcohol cross coupling

Butanol, benzylamine dehydrogenation, and butyraldehyde/primary imine-benzylamine coupling reactions compete with each other on cobalt oxide (Co_3O_4-350-B) when toluene was replaced with butanol (**Table 6**). Mn-Co_3O_4-250/350, G-Co_3O_4-350, and Cu-Co_3O_4-350 promote oxidation of butanol to butanal than benzylamine to benzaldehyde which leads to higher selectivity of the cross-coupled product. At the beginning of the reaction (2 h), butanol oxidation becomes more prominent

than benzylamine oxidation (**Figure 11**) which leads to higher rates of cross-coupled product formation (selectivity 82%). The steric advantage of butanol compared to benzylamine allows competitive butanol binding on active sites which explains the aforementioned rate changes. Mass transfer limitations kicked in (masking true kinetics) after 12 hours of reaction time yielding a plateau in the conversion curve. The plateau after 110°C (8 h reaction time) in **Figure 12** indicates active site reaction limited kinetics and mass transfer free reaction at elevated temperatures (>110°C). The increase in the selectivity of the cross-coupled product with the increase in the butanol volume up to 6 mL (**Figure 13**) suggest improved alcohol oxidation kinetics.

The increase in the cross-coupled product yield with low carbon number alcohols (**Table 7**) suggests size dependent competitive active site binding of alcohol and amines. Higher yield (93%) of butylamine-butanol (short-chain) cross-coupled product (**Table 8**) also suggest above size dependability. In the above case, the instability of aliphatic amine (compared to benzylic) derived intermediates may have led to decrease amount of homo-coupled product yield.

5. Understanding the reaction mechanism

Benzylamine homocoupling reactions have been carried out under thermal and photocatalytic conditions in the literature.[56,57,58] During both photo- and thermal-catalysis, benzylamine undergo dehydrogenation to form the intermediate primary imine which then transforms to benzaldehyde via hydrolysis or bond rearrangements. The fundamental difference between two mechanisms (thermal and photo) is the way the molecular oxygen participates in the reaction. In most thermal catalytic mechanisms, molecular oxygen participate during the catalytic regeneration step[59,60] whereas in photocatalytic reactions, oxygen (singlet) can directly contribute to the benzylamine to benzaldehyde conversion step.[61] Benzaldehyde formed via above mechanisms can couple with another molecule of benzylamine to yield secondary imine. During the cross-coupling reaction, alcohol first undergo oxidative dehydrogenation to form aldehyde which reacts with amine to form secondary imine.

Progress of the tandem reaction with higher selectivity toward the homo-coupled product (70 %, 24 h) even under an inert atmosphere (He) suggests higher contribution from the stoichiometric thermal mechanism on the homocoupling reaction under inert conditions (**Table 9**). However, the above observation does not suggest that the homocoupling reaction should only proceed through

the thermal mechanism. This merely suggests that under inert conditions reaction can continue through the thermal mechanism. Molar calculations revealed the presence of 0.083 mmol Co^{3+}, 0.041 mmol Co^{2+}, 0.049 mmol atomic oxygen, and 0.1 mmol benzylamine in the reactor vessel. If the reaction proceeds through a Mars-van Krevelen type mechanism (thermal), under inert atmosphere, only the existing Co^{3+} (0.083 mmol) amount should participate in the reaction and Co^{3+} should not be regenerated. Therefore, the theoretical homo-coupling yield should be around 83% (assuming all Co^{3+} stoichiometrically participate in the reaction and no trace oxygen) under inert conditions. Deviation (70%) from the theoretical yield (83%) can be attributed to the unexposed Co^{3+} sites and competitive cross-coupling reaction. Even though the maximum conversion (97%) was seen under molecular oxygen, selectivity towards homo-coupled product was slightly decreased (88%) due to overoxidized product formation. The decrease in the benzylamine conversion under CO_2 and NH_3 environments can be described in terms of active site (Lewis and Bronsted sites) poisoning.[62] Insignificant CC product selectivities (~1%) in the reflux system (**Table 9**) compared to the closed system (~50%; **Figure 11**) proposes an involvement of system pressure in the reaction. Similar pressure dependent product yields were observed in the experiment reported in **Figure 13**, which was done in 25 mL (higher volume, low pressure) vessel.

The EPR spectrum (**Figure 14a**) of spinel cobalt oxide resembles the tetrahedrally (high spin) coordinated Co^{2+} (S=3/2) complexes.[63] Since the low spin octahedral Co^{3+} (S=0) species are EPR silent and high spin tetrahedral/octahedral Co^{3+} are rare, Co^{2+} species should be responsible for the features in the EPR signal.[64] The decrease in the intensity of EPR signal indicates oxidation of Co^{2+} in the bulk of the catalyst as the reaction progress. On the contrary, post-catalyst XPS data show a higher Co^{2+}/Co^{3+} ratio than pre-catalyst (**Figure 15**) suggesting either an increase in the Co^{2+} concentration or/and a decrease in Co^{3+} concentration on the surface of the used catalyst. The aforementioned contradiction can be explained by looking at the reactions happening on the surface and in the bulk of the catalyst. Benzylamine can convert to benzaldehyde on Co (III) sites eventually generating Co (II) and oxygen vacancies on the surface of the catalyst (**Figure 18**). In the meantime, Co (II) can be oxidized to Co (III) in the bulk (charge balance) by accepting oxygen (by vacancy sites) from molecular oxygen (similar to Mars-van Krevelen type mechanism). Due to dimensional restrictions, the probability of butanol and benzylamine reaching the bulk of the crystallites is minimal whereas gaseous molecules (oxygen) can reach the bulk of the catalyst and

promote the Co^{2+} oxidation. Electrons released from benzylamine can be accepted by Co^{3+} on the surface (reduction) and electrons released during the Co^{2+} to Co^{3+} oxidation in the deep layers can be accepted by molecular oxygen.

Extremely low homo-coupled product selectivity (8%) and higher cross-coupled product selectivity (87%) in the presence of a singlet oxygen scavenger suggests crucial role of $^1O_2$ during the (thermal, low intensity light) homo-coupling reaction (**Table 10**). Singlet oxygen can be originated photochemically or thermally in the presence of a sensitizer or a proper precursor respectively.[65,66] Photochemically generated singlet oxygen-mediated amine to imine transformation (homocoupling only) has been reported in the literature.[67,68] However, use of an inorganic scavenger to promote cross-coupling reaction over the homocoupling reaction has not been reported. When it is required to synthesize homo-coupled product one can add mannitol to the reaction medium and sodium azide can be used when the CC product is required. Ammonium oxalate hole scavenger test also supports hole generation process even under low intensity photo-irradiation which indirectly suggests an electronic excitation during the reaction (**Table 10**). Increase in the product yield (94% homo-coupled) with the decrease in reaction time (from 24 to 8 h) under high intensity visible light (photoreactor) further support the singlet oxygen mediated reaction pathway (**Table 4**). Decrease in the homo-coupled product yield (42%, **Table 4**) under dark condition supports the low intensity photoexcitation of cobalt oxide. Even though an electronic excitation and involvement of singlet oxygen during homo-coupling reaction are clear, above mechanism dose not explain the considerable homo-coupled product yield (70%) observed under inert atmosphere (**Table 9**). As mentioned early in this section, under inert conditions, probably the reaction proceeds through a stoichiometric pathway. Even though high intensity photo-irradiation improved the reaction kinetics, considering the reaction being completed at 24 h under thermal (low intensity light) conditions, thermal-catalysis is the major contributor during the tandem reaction. High intensity photoirradiation is only assisting the singlet oxygen generation process.

Even though the mannitol test hints involvement of hydroxyl radicals in the alcohol-benzylamine cross-coupling reaction, further investigations are underway to understand the alcohol oxidation mechanisms. The discrepancy between the results of two hydroxyl scavengers, mannitol (CC selectivity 58%) and tert-butyl alcohol (CC selectivity 6%) could be a result of scavenger

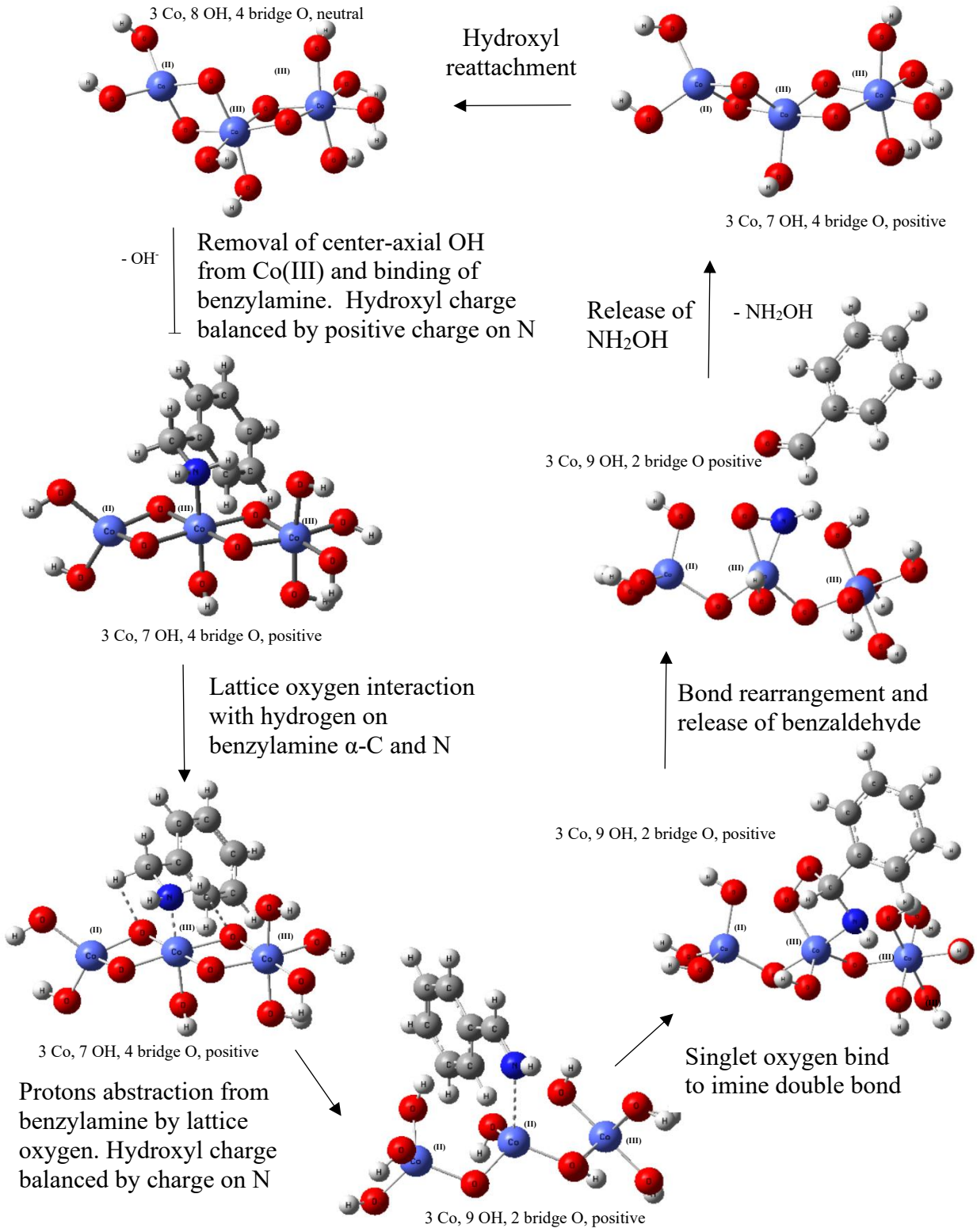

Figure 18. Proposed benzylamine to benzaldehyde conversion reaction mechanism

(also an alcohol) interference during the reaction. Increase of the conversion in the presence of TEMPO can be attributed to TEMPO mediated alcohol and benzylamine oxidation.[69] Extreme caution should be exercise when interpreting the ROS scavenger test results due to above complications.

Considering the ROS scavenger tests, EPR, and XPS data, a detailed benzylamine to benzaldehyde reaction mechanism has been proposed as shown in **Figure 18**. In the first step of the reaction, an axial hydroxyl group can be released from the Co (III) center generating a positive charge on the active site. The amine group of the benzylamine can interact with a high charge density Co (III) center than a Co (II) site creating a positive charge on the nitrogen. After the anchoring step, nearby lattice oxygens can abstract protons from the benzylamine (NH and CH) creating a cobalt (II) anchored primary imine. Singlet molecular oxygen can bind to imine making intermediate (N-Co-OO-C) species[61] (**Figure 20**) which eventually undergo bond rearrangement to make benzaldehyde. The cobalt site releases hydroxylamine by abstracting two protons from surface

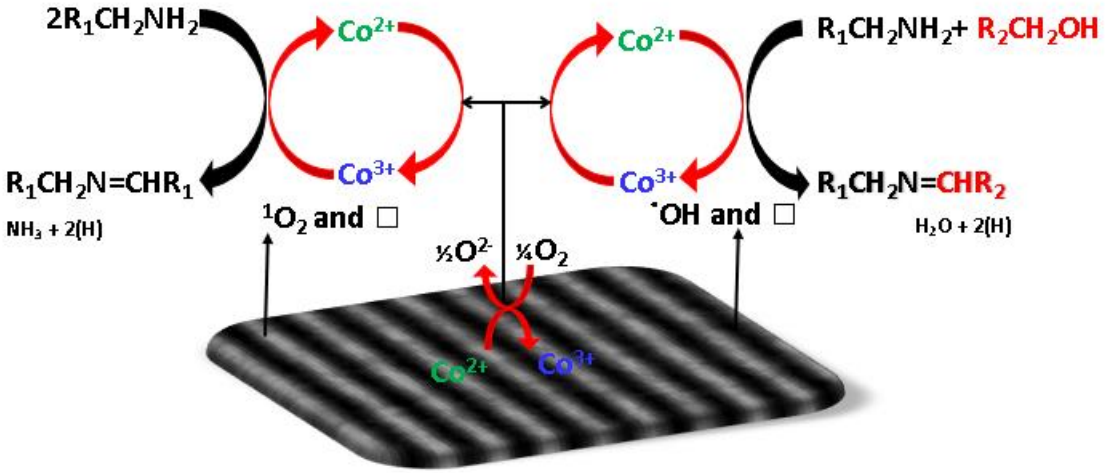

Figure 19. Participation of reactive oxygen species in the benzylamine homo and cross-coupling reactions (□ – holes, (H) – lattice hydrogens) under photo-assisted thermal catalysis

hydroxyl groups which regenerates bridging oxygen bonds. Slightly lower XPS peak area ratio of lattice oxygen to hydroxyl in post-catalyst (0.729) than the pre-catalyst (0.736) further supports the proposed mechanism in **Figure 18**. Water generated from the benzylamine-benzaldehyde coupling and hydroxyl condensation reactions can bind to the vacant sites (**Figure 15;** adsorbed water in used catalyst) created during Co^{3+} to Co^{2+} reduction. Role of reactive oxygen species

scavengers on the tandem reaction has been summarized in **Figure 19**. Overall, plausible reaction mechanism

Photo/thermally-excited electrons in the conduction band of cobalt oxide transfer to triplet oxygen creating superoxide radicals (**Figure 20)**. Electrons in the superoxide radicals transfer to previously formed holes forming singlet oxygens.[68,70] The activated singlet oxygen then participates in the cobalt-oxygen-amine intermediate formation which subsequently undergo rearrangement to benzaldehyde. In the absence of singlet oxygen, benzaldehyde ca n be formed via hydrolysis of the primary imine. Note the fate and role of oxygen atoms in the reaction.

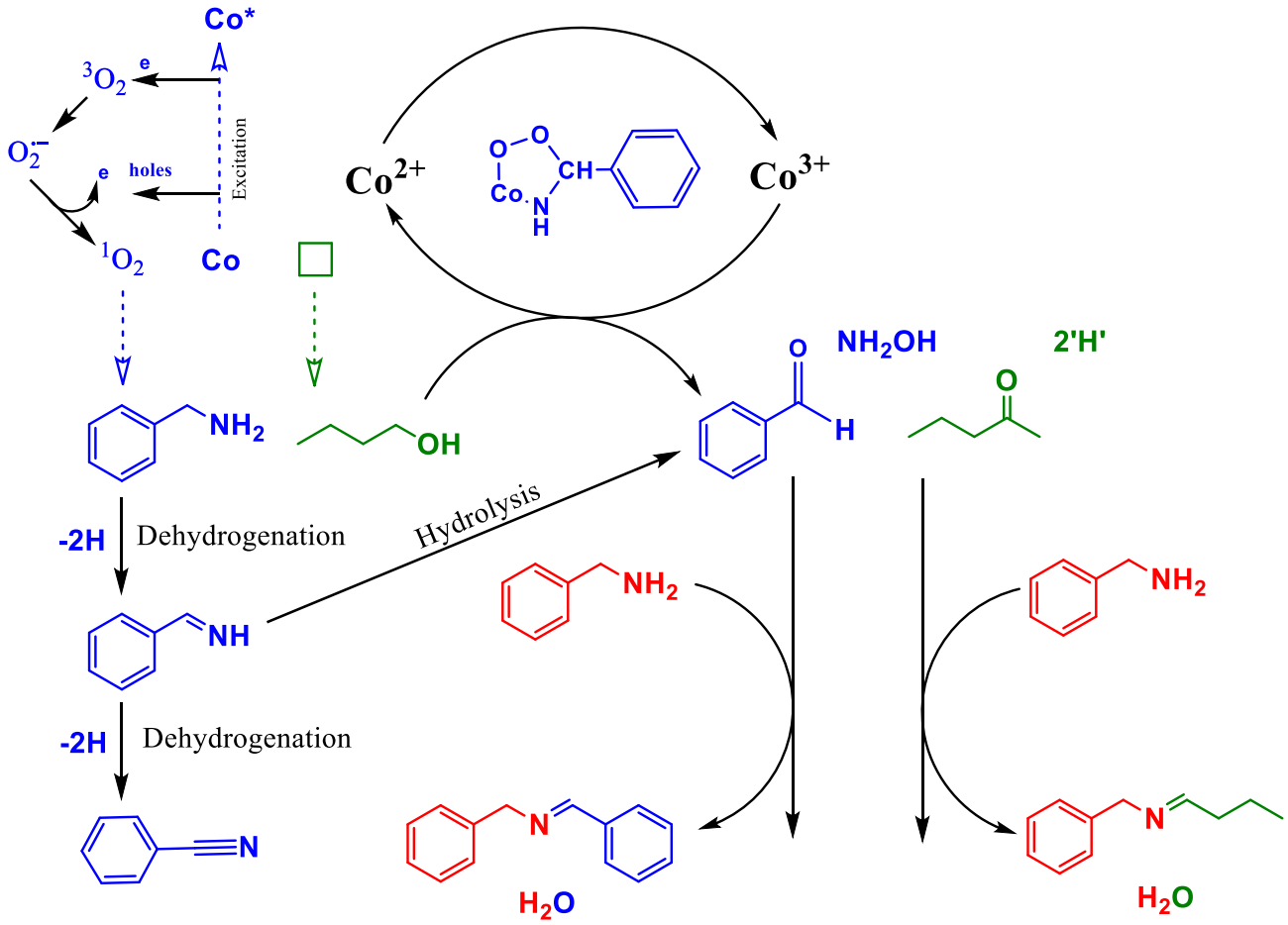

Figure 20. Complete plausible reaction mechanism based on observed reaction intermediates, products, and reactive oxygen species test

Conclusions

A series of nonionic surfactants with different chemical compositions were used to synthesize mesoporous cobalt oxide with monomodal fine-tuned pore size (9.6 nm-17.6 nm) distributions. Benzylamine homo-coupling reaction was used as a model reaction to determine the effect of surfactants on the chemical state of spinel cobalt oxide. Influences of crystallite size, morphology, surface area, pore size, and lattice oxygen content on the reactivity were established. The substrate scope study showed a steric hindrance effect on the homocoupling reaction suggesting site-specific binding of the substrate on the catalytic surface. A tandem, low-intensity photo-assisted amine homocoupling (mediated by singlet oxygen) and amine-alcohol hetero-coupling (mediated hydroxyl radical/holes) reaction strategy were introduced. Pseudo-second order reaction kinetics with an activation energy of 88 kJ/mol was observed. A reaction mechanism involving hydroxyl radical and singlet oxygen was proposed based on the EPR, XPS, and other experimental observations. Other than the reaction time and temperature, one can use singlet oxygen scavengers to control the product yields from benzylamine cross coupling and homo-coupling.

Declaration of Competing Interest

Declarations of interest: none

Acknowledgments

All authors are grateful for the financial support of the U.S. Department of Energy, Office of Basic Energy Sciences, Division of Chemical, Biological and Geological Sciences under Grant DE-FG02- 86ER13622. Biosciences Electron Microscopy Facility of the University of Connecticut and UConn/FEI Center for Advanced Microscopy and Materials Analysis (CAMMA) for SEM and TEM facilities.

References

(1) Zhu, B.; Lazar, M.; Trewyn, B. G.; Angelici, R. J. Aerobic Oxidation of Amines to Imines Catalyzed by Bulk Gold Powder and by Alumina-Supported Gold. *J. Catal.* **2008**, *260* (1), 1–6.

(2) Mitkina, T.; Stanglmair, C.; Setzer, W.; Gruber, M.; Kisch, H.; König, B. Visible Light Mediated Homo- and Heterocoupling of Benzyl Alcohols and Benzyl Amines on

Polycrystalline Cadmium Sulfide. *Org. Biomol. Chem.* **2012**, *10* (17), 3556–3561.

(3) Berger, D. Understanding Organic Reaction Mechanisms (Jacobs, Adam). *J. Chem. Educ.* **1999**, *76* (2), 167.

(4) Largeron, M. Protocols for the Catalytic Oxidation of Primary Amines to Imines. *European J. Org. Chem.* **2013**, *2013* (24), 5225–5235.

(5) Tian, H.; Yu, X.; Li, Q.; Wang, J.; Xu, Q. General, Green, and Scalable Synthesis of Imines from Alcohols and Amines by a Mild and Efficient Copper-Catalyzed Aerobic Oxidative Reaction in Open Air at Room Temperature. *Adv. Synth. Catal.* **2012**, *354* (14–15), 2671–2677.

(6) Chen, B.; Wang, L.; Gao, S. Recent Advances in Aerobic Oxidation of Alcohols and Amines to Imines. *ACS Catalysis.* **2015**, *5*(10), 5851–5876.

(7) Adams, J. P. Imines, Enamines and Oximes. *Journal of the Chemical Society, Perkin Transactions 1*. **2000**, 125–139.

(8) Sharma, H.; Singh, N.; Jang, D. O. A Ball-Milling Strategy for the Synthesis of Benzothiazole, Benzimidazole and Benzoxazole Derivatives under Solvent-Free Conditions. *Green Chem.* **2014**, *16* (12), 4922–4930.

(9) Patil, R. D.; Adimurthy, S. Copper(0)-Catalyzed Aerobic Oxidative Synthesis of Imines from Amines under Solvent-Free Conditions. *RSC Adv.* **2012**, *2* (12), 5119–5122.

(10) Makwana, V. D.; Son, Y. C.; Howell, A. R.; Suib, S. L. The Role of Lattice Oxygen in Selective Benzyl Alcohol Oxidation Using OMS-2 Catalyst: A Kinetic and Isotope-Labeling Study. *J. Catal.* **2002**, *210* (1), 46–52.

(11) Kumar, R.; Sithambaram, S.; Suib, S. L. Cyclohexane Oxidation Catalyzed by Manganese Oxide Octahedral Molecular Sieves-Effect of Acidity of the Catalyst. *J. Catal.* **2009**, *262* (2), 304–313.

(12) Shaabani, A.; Mirzaei, P.; Naderi, S.; Lee, D. G. Green Oxidations. The Use of Potassium Permanganate Supported on Manganese Dioxide. *Tetrahedron* **2004**, *60* (50), 11415–

11420.

(13) Largeron, M. Protocols for the Catalytic Oxidation of Primary Amines to Imines. *European J. Org. Chem.* **2013**, *2013* (24), 5225–5235.

(14) Xiao, J.; Kuang, Q.; Yang, S.; Xiao, F.; Wang, S.; Guo, L. Surface Structure Dependent Electrocatalytic Activity of Co_3O_4 Anchored on Graphene Sheets toward Oxygen Reduction Reaction. *Sci. Rep.* **2013**, *3* (1), 2300.

(15) Khodakov, A. Y.; Chu, W.; Fongarland, P. Advances in the Development of Novel Cobalt Fischer-Tropsch Catalysts for Synthesis of Long-Chain Hydrocarbons and Clean Fuels. *Chemical Reviews*. **2007**, *107*(5), 1692–1744.

(16) Liu, Y. C.; Koza, J. A.; Switzer, J. A. Conversion of Electrodeposited $Co(OH)_2$ to CoOOH and Co_3O_4, and Comparison of Their Catalytic Activity for the Oxygen Evolution Reaction. *Electrochim. Acta* **2014**, *140*, 359–365.

(17) Zhu, J.; Kailasam, K.; Fischer, A.; Thomas, A. Supported Cobalt Oxide Nanoparticles as Catalyst for Aerobic Oxidation of Alcohols in Liquid Phase. *ACS Catal.* **2011**, *1* (4), 342–347.

(18) Iosub, A. V.; Stahl, S. S. Catalytic Aerobic Dehydrogenation of Nitrogen Heterocycles Using Heterogeneous Cobalt Oxide Supported on Nitrogen-Doped Carbon. *Org. Lett.* **2015**, *17* (18), 4404–4407.

(19) Zhang, G.; Hanson, S. K. Cobalt-Catalyzed Acceptorless Alcohol Dehydrogenation: Synthesis of Imines from Alcohols and Amines. *Org. Lett.* **2013**, *15* (3), 650–653.

(20) Shiraishi, Y.; Ikeda, M.; Tsukamoto, D.; Tanaka, S.; Hirai, T. One-Pot Synthesis of Imines from Alcohols and Amines with TiO_2 Loading Pt Nanoparticles under UV Irradiation. *Chem. Commun.* **2011**, *47* (16), 4811–4813.

(21) Kwon, M. S.; Kim, S.; Park, S.; Bosco, W.; Chidrala, R. K.; Park, J. One-Pot Synthesis of Imines and Secondary Amines by Pd-Catalyzed Coupling of Benzyl Alcohols and Primary Amines. *J. Org. Chem.* **2009**, *74* (7), 2877–2879.

(22) Den Breejen, J. P.; Radstake, P. B.; Bezemer, G. L.; Bitter, J. H.; Frøseth, V.; Holmen, A.; De Jong, K. P. On the Origin of the Cobalt Particle Size Effects in Fischer-Tropsch Catalysis. *J. Am. Chem. Soc.* **2009**, *131* (20), 7197–7203.

(23) Liu, X.; Zhang, L.; Zheng, Y.; Guo, Z.; Zhu, Y.; Chen, H.; Li, F.; Liu, P.; Yu, B.; Wang, X.; et al. Uncovering the Effect of Lattice Strain and Oxygen Deficiency on Electrocatalytic Activity of Perovskite Cobaltite Thin Films. *Adv. Sci.* **2019**, *6* (6), 1801898.

(24) Pope, D.; Walker, D. S.; Moss, R. L. Preparation of Cobalt Oxide Catalysts and Their Activity for CO Oxidation at Low Concentration. *J. Catal.* **1977**, *47* (1), 33–47.

(25) Mogudi, B. M.; Ncube, P.; Meijboom, R. Catalytic Activity of Mesoporous Cobalt Oxides with Controlled Porosity and Crystallite Sizes: Evaluation Using the Reduction of 4-Nitrophenol. *Appl. Catal. B Environ.* **2016**, *198*, 74–82.

(26) Poyraz, A. S.; Kuo, C. H.; Biswas, S.; King'ondu, C. K.; Suib, S. L. A General Approach to Crystalline and Monomodal Pore Size Mesoporous Materials. *Nat. Commun.* **2013**, *4*, 3952.

(27) Wan, Y.; Shi, Y.; Zhao, D. Designed Synthesis of Mesoporous Solids via Nonionic-Surfactant-Templating Approach. *Chem. Commun.* **2007**, *0* (9), 897–926.

(28) Kim, D. S.; Han, S. J.; Kwak, S. Y. Synthesis and Photocatalytic Activity of Mesoporous TiO_2 with the Surface Area, Crystallite Size, and Pore Size. *J. Colloid Interface Sci.* **2007**, *316* (1), 85–91.

(29) Wang, Y. de; Ma, C. L.; Sun, X. D.; Li, H. De. Preparation of Nanocrystalline Metal Oxide Powders with the Surfactant-Mediated Method. *Inorg. Chem. Commun.* **2002**, *5* (10), 751–755.

(30) Khorsand Zak, A.; Abd. Majid, W. H.; Abrishami, M. E.; Yousefi, R. X-Ray Analysis of ZnO Nanoparticles by Williamson-Hall and Size-Strain Plot Methods. *Solid State Sci.* **2011**, *13* (1), 251–256.

(31) Sastry, N. V.; Valand, M. K. Densities, Viscosities, and Relative Permittivities for Pentane + 1-Alcohols (C 1 to C 12) at 298.15 K. *J. Chem. Eng. Data* **2002**, *43* (2), 152–157.

(32) ALOthman, Z. A Review: Fundamental Aspects of Silicate Mesoporous Materials. *Materials (Basel).* **2012**, *5* (12), 2874–2902.

(33) Matthias Thommes, S.; Cychosz, K. A.; my Guillet-Nicolas, R.; Garcí a-Martí nez, J.; Thommes, M. As Featured in: Recent Advances in the Textural Characterization of Hierarchically Structured Nanoporous Materials. *Chem. Soc. Rev. Chem. Soc. Rev* **2017**, *46* (46), 389–414.

(34) Jiang, C. M.; Baker, L. R.; Lucas, J. M.; Vura-Weis, J.; Alivisatos, A. P.; Leone, S. R. Characterization of Photo-Induced Charge Transfer and Hot Carrier Relaxation Pathways in Spinel Cobalt Oxide (Co_3O_4). *J. Phys. Chem. C* **2014**, *118* (39), 22774–22784.

(35) Taghavimoghaddam, J.; Knowles, G. P.; Chaffee, A. L. Preparation and Characterization of Mesoporous Silica Supported Cobalt Oxide as a Catalyst for the Oxidation of Cyclohexanol. *J. Mol. Catal. A Chem.* **2012**, *358*, 79–88.

(36) Pal, M.; Singh, A. K.; Rakshit, R.; Mandal, K. Surface Chemistry Modulated Introduction of Multifunctionality within Co_3O_4 Nanocubes. *RSC Adv.* **2015**, *5* (21), 16311–16318.

(37) Singh, V.; Major, D. T. Electronic Structure and Bonding in Co-Based Single and Mixed Valence Oxides: A Quantum Chemical Perspective. *Inorg. Chem.* **2016**, *55* (7), 3307–3315.

(38) Dai, G.; Liu, S.; Liang, Y.; Luo, T. Synthesis and Enhanced Photoelectrocatalytic Activity of P-n Junction Co_3O_4 /TiO_2 Nanotube Arrays. *Appl. Surf. Sci.* **2013**, *264*, 157–161.

(39) Tomon, C.; Sarawutanukul, S.; Duangdangchote, S.; Krittayavathananon, A.; Sawangphruk, M. Photoactive Zn-Air Batteries Using Spinel-Type Cobalt Oxide as a Bifunctional Photocatalyst at the Air Cathode. *Chem. Commun.* **2019**, *55* (42), 5855–5858.

(40) Deng, S.; Chen, N.; Deng, D.; Li, Y.; Xing, X.; Wang, Y. Meso- and Macroporous Coral-like Co_3O_4 for VOCs Gas Sensor. *Ceram. Int.* **2015**, *41* (9), 11004–11012.

(41) Zhang, L.; Zhao, X.; Ma, W.; Wu, M.; Qian, N.; Lu, W. Novel Three-Dimensional Co_3O_4 Dendritic Superstructures: Hydrothermal Synthesis, Formation Mechanism and Magnetic Properties. *CrystEngComm* **2013**, *15* (7), 1389–1396.

(42) Cho, S. H.; Jung, J. W.; Kim, C.; Kim, I. D. Rational Design of 1-D Co_3O_4 Nanofibers@Low Content Graphene Composite Anode for High Performance Li-Ion Batteries. *Sci. Rep.* **2017**, *7* (1), 45105.

(43) Zhang, L.; Zhao, X.; Ma, W.; Wu, M.; Qian, N.; Lu, W. Novel Three-Dimensional Co_3O_4 Dendritic Superstructures: Hydrothermal Synthesis, Formation Mechanism and Magnetic Properties. *CrystEngComm* **2013**, *15* (7), 1389–1396.

(44) Tan, Y.; Gao, Q.; Yang, C.; Yang, K.; Tian, W.; Zhu, L. One-Dimensional Porous Nanofibers of Co_3O_4 on the Carbon Matrix from Human Hair with Superior Lithium Ion Storage Performance. *Sci. Rep.* **2015**, *5* (1), 12382.

(45) Zhang, X.; Chen, Y. S.; Kamat, P. V.; Ptasinska, S. Probing Interfacial Electrochemistry on a Co_3O_4 Water Oxidation Catalyst Using Lab-Based Ambient Pressure X-Ray Photoelectron Spectroscopy. *J. Phys. Chem. C* **2018**, *122* (25), 13894–13901.

(46) Paulraj, A. R.; Kiros, Y. $La_{0.1}Ca_{0.9}MnO_3/Co_3O_4$ for Oxygen Reduction and Evolution Reactions (ORER) in Alkaline Electrolyte. *J. Solid State Electrochem.* **2018**, *22* (6), 1697–1710.

(47) Xu, J.; Gao, P.; Zhao, T. S. Non-Precious Co_3O_4 Nano-Rod Electrocatalyst for Oxygen Reduction Reaction in Anion-Exchange Membrane Fuel Cells. *Energy Environ. Sci.* **2012**, *5* (1), 5333–5339.

(48) Sun, X.; Jiang, Z.; Li, C.; Jiang, Y.; Sun, X.; Tian, X.; Luo, L.; Hao, X.; Jiang, Z. J. Facile Synthesis of Co_3O_4 with Different Morphologies Loaded on Amine Modified Graphene and Their Application in Supercapacitors. *J. Alloys Compd.* **2016**, *685*, 507–517.

(49) Chan, D.; Tischer, S.; Heck, J.; Diehm, C.; Deutschmann, O. Correlation between Catalytic Activity and Catalytic Surface Area of a Pt/Al_2O_3 DOC: An Experimental and Microkinetic Modeling Study. *Appl. Catal. B Environ.* **2014**, *156–157*, 153–165.

(50) Pu, S. Bin. Influence of Crystallite Size on Catalytic Performance of HZSM-5 Prepared by Different Methods in 2,7-Dimethylnaphthalene Isomerization. *Zeolites* **1996**, *17* (4), 334–339.

(51) Iwamoto, M.; Tanaka, Y.; Sawamura, N.; Namba, S. Remarkable Effect of Pore Size on the Catalytic Activity of Mesoporous Silica for the Acetalization of Cyclohexanone with Methanol. *J. Am. Chem. Soc.* **2003**, *125* (43), 13032–13033.

(52) Morales, S.; Guijarro, F. G.; García Ruano, J. L.; Cid, M. B. A General Aminocatalytic Method for the Synthesis of Aldimines. *J. Am. Chem. Soc.* **2014**, *136* (3), 1082–1089.

(53) Liu, L.; Zhang, S.; Fu, X.; Yan, C. H. Metal-Free Aerobic Oxidative Coupling of Amines to Imines. *Chem. Commun.* **2011**, *47* (36), 10148–10150.

(54) Chu, G.; Li, C. Convenient and Clean Synthesis of Imines from Primary Benzylamines. *Org. Biomol. Chem.* **2010**, *8* (20), 4716–4719.

(55) Edmondson, D. E.; Binda, C.; Mattevi, A. Structural Insights into the Mechanism of Amine Oxidation by Monoamine Oxidases A and B. *Archives of Biochemistry and Biophysics*. **2007**, *464*(2), 269–276.

(56) Lang, X.; Ji, H.; Chen, C.; Ma, W.; Zhao, J. Selective Formation of Imines by Aerobic Photocatalytic Oxidation of Amines on TiO_2. *Angew. Chemie Int. Ed.* **2011**, *50* (17), 3934–3937.

(57) Zhao, W.; Liu, C.; Cao, L.; Yin, X.; Xu, H.; Zhang, B. Porous Single-Crystalline CdS Nanosheets as Efficient Visible Light Catalysts for Aerobic Oxidative Coupling of Amines to Imines. *RSC Adv.* **2013**, *3* (45), 22944–22948.

(58) Patil, R. D.; Adimurthy, S. Copper(0)-Catalyzed Aerobic Oxidative Synthesis of Imines from Amines under Solvent-Free Conditions. *RSC Adv.* **2012**, *2* (12), 5119–5122.

(59) Tamura, M.; Tomishige, K. Redox Properties of CeO_2 at Low Temperature: The Direct Synthesis of Imines from Alcohol and Amine. *Angew. Chemie Int. Ed.* **2015**, *54* (3), 864–867.

(60) Furukawa, S.; Suga, A.; Komatsu, T. Highly Efficient Aerobic Oxidation of Various Amines Using Pd_3Pb Intermetallic Compounds as Catalysts. *Chem. Commun.* **2014**, *50* (25), 3277–3280.

(61) Zhai, Z. Y.; Guo, X. N.; Jin, G. Q.; Guo, X. Y. Visible Light-Induced Selective Photocatalytic Aerobic Oxidation of Amines into Imines on Cu/Graphene. *Catal. Sci. Technol.* **2015**, *5* (8), 4202–4207.

(62) Sithambaram, S.; Kumar, R.; Son, Y. C.; Suib, S. L. Tandem Catalysis: Direct Catalytic Synthesis of Imines from Alcohols Using Manganese Octahedral Molecular Sieves. *J. Catal.* **2008**, *253* (2), 269–277.

(63) Tachibana, M.; Iwaizumi, M.; Tero-Kubota, S. EPR Studies of Copper(II) and Cobalt(II) Complexes of Adriamycin. *J. Inorg. Biochem.* **1987**, *30* (2), 133–140.

(64) Barrett, P. A.; Sankar, G.; Richard, C.; Callow, A.; Thomas, J. M. X-Ray Absorption Spectroscopic Study of Brøns Ted, Lewis, and Redox Centers in Cobalt-Substituted Aluminum Phosphate Catalysts. *J. Phys. Chem.* **1996**, *100* (21), 8977–8985.

(65) Ashen-Garry, D.; Selke, M. Singlet Oxygen Generation by Cyclometalated Complexes and Applications. *Photochemistry and Photobiology*. **2014**, 90(*2*), 257–274.

(66) Guillory, J. P.; Shiblom, C. M. The Generation of Singlet Oxygen by a Lithium-Tin-Phosphorus Catalyst. *J. Catal.* **1978**, *54* (1), 24–30.

(67) Jiang, G.; Chen, J.; Huang, J. S.; Che, C. M. Highly Efficient Oxidation of Amines to Imines by Singlet Oxygen and Its Application in Ugi-Type Reactions. *Org. Lett.* **2009**, *11* (20), 4568–4571.

(68) Ovoshchnikov, D. S.; Donoeva, B. G.; Golovko, V. B. Visible-Light-Driven Aerobic Oxidation of Amines to Nitriles over Hydrous Ruthenium Oxide Supported on TiO_2. *ACS Catal.* **2015**, *5* (1), 34–38.

(69) Ciriminna, R.; Ghahremani, M.; Karimi, B.; Pagliaro, M. Electrochemical Alcohol Oxidation Mediated by TEMPO-like Nitroxyl Radicals. *ChemistryOpen*. **2017**, *6*(1), 5–10.

(70) Nosaka, Y.; Daimon, T.; Nosaka, A. Y.; Murakami, Y. Singlet Oxygen Formation in Photocatalytic TiO_2 aqueous Suspension. *Phys. Chem. Chem. Phys.* **2004**, *6* (11), 2917–2918.

Graphical abstract